CHAPTER 1.

Literature Review: Thermoplastic Composite Materials.

1.0 Abstract.

Polymer composites are playing an increasing role as construction materials in a wide variety of applications. In particular, thermoplastic polymer composites are falling under increasing scrutiny due to their potential to be easily repaired and/or reshaped, making them easier to recycle and reuse compared with thermosetting matrix composites.

Thermoplastic composite materials, like thermosetting polymer composites, frequently suffer from a lack of fiber-matrix adhesion. This is typically remedied using fiber surface modification. Chemical modification or the addition of a third, compatibilizing phase bridging the fiber and matrix phases has been successfully applied to improving the interfacial characteristics of many polymer composite systems. Another problem encountered during the production of thermoplastic composites is quality of consolidation. Hot pressing is typically employed to obtain a uniform distribution of matrix material around the reinforcing fiber, remove voids, as well as bring about sufficient contact between the fiber and matrix.

Biobased composite systems are a class of polymer composites that seek to remedy the issues regarding raw material sources as well as disposal at the end of the product life cycle. In particular, lignocellulosic biomass represents a large and renewable source of polymeric raw materials. A new class of biobased composites is currently under study at the Biobased Materials/Recycling Center of Virginia Tech. Cellulosic polymers in this case serve as both thermoplastic matrix and fiber reinforcement. In this study, the interfacial characteristics are to be examined as well as the consolidation behavior of the composite during hot pressing.

The aims of this study are to determine whether or not there is a lack of fiber/matrix adhesion and if so, to determine whether or not fiber surface acetylation remedies this problem. Afterwards, consolidation will be examined over a range of times, temperatures and pressures to determine the condition(s) at which void content is minimized and interlaminar shear strength is maximized.

1.1 Introduction to Polymer Composites.

Polymer composites are increasingly gaining importance as substitute materials for metals in applications within the aerospace, automotive, marine, sporting goods and electronic industries. Their light weight and superior mechanical properties make them especially suited for transportation applications.

Fibrous composite materials typically have two or more distinct phases, which include high strength/stiffness reinforcing fibers and the encapsulating matrix material. Fibers can be either discontinuous (chopped) or continuous. Polymer matrices typically fall into two categories: thermoplastic and thermosetting polymers. Thermoplastic polymers are distinguished by their ability to be reshaped upon the addition of heat (above the glass transition temperature of the amorphous phase or the melting temperature of the crystalline phase). This cycle can be carried out repeatedly. Thermosetting polymers, on the other hand, undergo chemical reactions during curing which crosslink the polymer molecules. Once crosslinked, thermosets become permanently hard and simply undergo chemical decomposition under the application of excessive heat. Thermosetting polymers typically have greater abrasion resistance and dimensional stability over that of thermoplastic polymers, which typically have better flexural and impact properties.

1.2 Introduction to Thermoplastic Composite Materials.

Throughout the prior two decades, fiber reinforced composite materials were principally fabricated using thermosetting matrices [Hancox, 1989]. Disadvantages stemming from the use of thermosets include brittleness, lengthy cure cycles and inability to repair and/or recycle damaged or scrapped parts. These disadvantages led to the development of the thermoplastic matrix composite system. Compared with thermosets, composites fabricated from thermoplastic materials typically have a longer shelf life, higher strain to failure, are faster to consolidate and retain the ability to be repaired, reshaped and reused as need arises. However, as in many polymer composite systems, these materials frequently suffer from a lack of adequate fiber-matrix adhesion. In addition, the use of thermoplastics introduces the problem of adequate fiber tow penetration. Thermoplastic melts, as opposed to thermosetting resins, have a substantially higher viscosity. Thermoplastic matrices must be able to withstand high temperatures in order to effect a sufficient reduction in viscosity. Additional problems caused by high matrix viscosity during consolidation include de-alignment of reinforcing fibers during consolidation as well as the introduction of voids within the final composite product [Bafna, 1991]. All of these problems can be addressed by appropriate design regarding the fiber-matrix interface as well as optimization of composite fabrication procedures. Composites prepared with satisfactory matrix dispersion within the fiber tows as well as reasonable fiber-matrix adhesive interaction typically results in composites with good mechanical properties.

1.3 Fabrication of Thermoplastic Composites: An Overview.

The first step in the design of a thermoplastic composite material is an appropriate choice of a fabrication method. There are several widely used methods to prepare thermoplastic composite materials, several of which are outlined below.

1.3.0 Solution Impregnation.

The solubility of thermoplastics as opposed to thermosetting materials has led to the use of solution deposition and impregnation of matrix material onto fiber tows. 'Solution prepregging' is a common technique used to fabricate thermoplastic composite materials [Cano and Marchello, 1995; Lacroix *et al*., 1998; Moon et al., 1992; Wu et al., 1990]. This process entails solubilizing the matrix polymer at a suitable concentration and then immersing the fiber tow within the solution. In the ideal case, the polymer solution will individually wet each filament within the fiber tow. Once the fiber has been coated with solution, the fiber article is then removed from solution and the solvent must be evaporated before further fabrication steps are taken. Prepreg tows are then conventionally arranged in sheet form after which they are consolidated in a hot press to produce a composite article.

1.3.1 Powder Impregnation/Pultrusion.

Another method of preparing composite preforms is powder-impregnation [Bucher and Hinkley, 1992; Yu and Davis, 1993]. In this case, the fabric or sheet reinforcement is impregnated with a suspension of fine (<5 micrometers) polymer particles [Hancox, 1989]. The prepregged sheet is then consolidated within a hot press. This method is restricted to polymer matrices that can be cryogenically ground to produce fine particles or precipitated from solution. Pultrusion operates in a similar manner. Fiber tow is pulled through powdered resin (30-250 micrometers) in a coating unit and then shaped and heated within a die. Pultruded tow is then arranged in sheet form and consolidated within a hot press.

1.3.2 Film Stacking.

Film stacking is a third technique with which to prepare thermoplastic composites [Mayer *et al*., 1998; Bafna and Baird, 1991]. In this case, fiber tows arranged in sheet form are sandwiched between matrix polymer films. This assembly is then placed within a press where temperature transforms the film into a polymer melt. Pressure is then applied and forces the melt to impregnate the fiber tow. Appropriate process conditions must be used in order to sufficiently reduce the matrix viscosity without thermally degrading the actual composite or de-align the fibrous reinforcement. Insufficient heat input and/or pressure will typically result in unwetted fiber and a high void content within the final material.

1.3.3 Consolidation of Thermoplastic Preforms.

After preparation, thermoplastic prepregs are then arranged in sheet form and stacked in either a unidirectional or cross-ply manner. This stack is then pressed within a mold under pressure and temperature. During pressing, a vacuum is frequently used in order to remove any air or solvents used to process the prepregs [Hancox, 1989]. The use of a vacuum during the final consolidation step can aid in the reduction of voids within the final composite article. Optimal process parameters, such as residence time, temperature and pressure must all be determined for the particular composite system and preform fabrication method.

1.4 Composite Manufacture by Solution Preimpregnation.

Because solution impregnation will be used as the method of manufacture in this work, the individual processing steps will be reviewed briefly in the following section. To review, solution prepregging consists of three principle steps: (1) application of polymer solution onto the reinforcing tows; (2) removal of solvent from the prepreg; and (3) consolidation of prepregs.

1.4.0 Wetting During Solution Prepregging.

Optimization of the solution prepregging process begins with the appropriate choice of solvent. A high degree of wetting can only be expected from solvents that possess favorable thermodynamics regarding wetting of the particular solid material (filaments, in this case). A common method for the examination of wetting thermodynamics is to measure the contact angle (Figure 1.0).

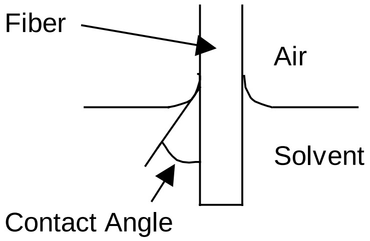

Figure 1.0 Contact Angle in a Fiber/Air/Solvent System.

The contact angle directly governs the process of wetting and the penetration of porous solids by liquids [Good, 1979]. The process of wetting entails the contact and spreading of the solvent over the surface of the solid, i.e., liquids that possess a low contact angle for a particular solid show considerable wetting behavior (as opposed to liquids that display high contact angles).

Using the Wilhelmy plate principle to measure contact angles, the difference between the weight of the fiber at the point of detachment ($W_{detachment}$) from the solid/ liquid interface and the weight of the fiber itself (W_{fiber}) is given by [Shaw, 1992]:

$$W_{\det achment} - W_{fiber} = P_{3-phase}\gamma_{LV}\cos\theta \qquad (1.0)$$

where: $P_{3\text{-}phase}$ = perimeter of the three phase boundary line

γ_{LV} = surface tension between the liquid and vapor phase

θ = equilibrium advancing contact angle

After the contact angle has been measured, the solvent with the lowest contact angle with respect to the solid can be identified. This solvent should be chosen from a list of candidate solvents capable of dissolving the matrix polymer. The differences in wetting action, coupled with other relevant parameters such as boiling point and general practicality of the particular solvent choice usage, will lead to an appropriate choice of solvent. In particular, solvent characteristics should include a much lower boiling point than melt flow point of the resin and a lower density then that of the resin (for ease of residual solvent removal during melt consolidation) [Moon *et al.*, 1993].

An example of the preceding contact angle analysis can be found in a study by Patel and Lee [1996]. In this study, fiberglass tows were subjected to contact angle analysis using the Wilhelmy plate method. A series of liquids was used (*not* polymer solutions), each having differing values of viscosity and surface tension. The equilibrium contact angles for all of these liquids were not observed to be a function of solvent viscosity (viscosity range = 0.33 mPa – 1499.0). Furthermore, the liquid surface tension was found to be positively correlated with the contact angle, i.e., increases in surface tension generally yielded larger contact angle measurements. It should be stressed that these results only indicate trends in contact angles; they may not imply favorable conditions for capillary flow (in addition to wetting), which is another important consideration in the prepreg process [Lee, 1996].

Once the appropriate solvent is identified for solution prepregging, prepregged tapes can be prepared. The objective in solution prepregging is to prepare a uniform tape in which every fiber surface is uniformly wetted with the polymeric matrix material. This concept will be further referred to as the *fiber dispersion*, generally examined using optical microscopy of the composite cross sections and quantified using image analysis techniques. Quantifiable variables of interest include the average inter-fiber radial distance, as well as the shape of the distribution. Another objective in solution prepregging is maximizing the *amount* of matrix material pick-up. This is easily quantifiable as the amount of matrix material adhering to the fiber surface after a single immersion into the solution bath.

The nature of the relationship between fiber dispersion and matrix pick up is expected to be competitive. This can be inferred from the extremes of the process. In a polymer solution with a concentration approaching zero, every filament can be expected to be wetted (resulting in a good fiber dispersion), assuming that the thermodynamics are favorable. But the matrix pick up in this case is nearly zero since there is no polymer in solution. At the other extreme, the polymer weight fraction in solution approaches one. In this case, the fiber dispersion upon fiber dipping will be very poor given the *extremely high* viscosity of the solution (kinetic limitation). But upon wetting, a large amount of polymer will remain on the fiber surface (high matrix pick up). Therefore, intuition states that there will exist an intermediate polymer solution concentration in which a balance is obtained between the fiber dispersion and matrix pick up.

The concepts in the preceding paragraph can be more easily visualized by using a model that approximates the wetting process of a fiber tow by a polymer solution. By combining the Kelvin equation, which describes wetting of a solution in micro-capillaries and Darcy's Law, which describes flow in porous media, the following equation is obtained:

$$t_f = l^2 \mu V_{void} / \{2S_b (2/R) \gamma_{sizing} \cos\theta\} \tag{1.1}$$

where: t_f = tow wetting time
l = tow thickness
μ = solution viscosity
V_{void} = tow void volume
S_b = tow permeability (perpendicular to fiber direction)
R = fiber-fiber separation
$\gamma_{solution}$ = solution surface tension
θ = contact angle

A quick survey of Eq. (1.1) reveals the following three trends:

- As the solution viscosity increases, the time of tow wetting increases.
- As the surface tension of the solution increases, the time of tow wetting decreases.
- As the contact angle increases from 0° (complete wetting) to 90° (mostly non-wetting), the cosine term decreases and thus increases the time of tow wetting.

Prepreg residence time is also known to influence both the fiber dispersion and efficiency. In a study by Lacroix *et al.* [1998], ultra-high modulus polyethylene fiber bundles were prepregged with a xylene/ low-density polyethylene solution. For a prepregging time range of 8 min. – 19.5 hours, it was noted that increasing prepreg time increased the layer thickness of deposited polymer around the fiber surfaces. Similar results were obtained in a study by Moon *et al.* [1993] in which solvent prepregged fiber bundles were prepared from glass fibers and a high-density polyethylene/ toluene solution.

1.4.1 Prepreg Solvent Removal.

After the fiber tapes are prepregged with solution, the solvent has to be driven off. In this case, since the tapes are not to be wound around a storage spool following prepregging, solvent elimination should be complete. This represents a crucial step in the overall composite manufacturing process, as residual solvent can result in voids during the melt consolidation process.

How the solvent interaction with the fiber/matrix interface is an important consideration, given the influence of the quality of the interface in determining the final mechanical properties of the composite. The presence of solvent is generally known to reduce the quality of the matrix/fiber interface. The reasons for this phenomenon are unclear, but can be explained by the following hypothesis [Smith *et al.*, 1996]:

- Solvent extraction can cause separation of the fiber/matrix interface
- Solvent concentration at the interface will interfere with fiber/matrix contact; and,
- Phase separation of low molecular weight species at the interface may form a weak interface between the fiber and matrix.

Solvent removal, in part, is regarded to proceed by solvent concentration at the interface, followed by solvent traversing the fiber surface and escaping from the ends of the composite. Obviously this will result in poor interfacial quality if this is to occur during melt consolidation.

A study conducted by Wu *et al.* [1990] illustrates how residual solvent negatively affects composite mechanical property quality. Solution prepregged carbon fiber reinforced polyethersulphone composites were prepared and compared with strictly hot-melt processed composites of the same nominal fiber content. The transverse flexural strength of the solution prepregged material was only half that of the melt-processed material. Upon analysis of the solution prepregged material using differential scanning calorimetry (DSC), it was found that residual solvent remained in the sample, *despite* hot-melt consolidation of the prepreg. Residual solvent can most likely be attributable to difficulty in solvent diffusion during the consolidation process. The reasons for poor interfacial quality are thought to be attributable in the reasons outlined in the preceding paragraph.

1.4.2 Hot Melt Consolidation of Prepregs.

Given that a uniform distribution of matrix material is desired in the final composite product, it is obvious that the optimization of melt consolidation physical parameters will be required. These parameters can include press temperature, press consolidation time and press pressure. Before any consideration can be given to fiber surface treatments, etc. to enhance adhesion, adequate consideration must be applied to first bringing the matrix within uniform contact in and around the fiber tow.

With most thermoplastic composite materials, press temperature considerably affects the mechanical properties of the composite produced. Bulk resin movement (in order to fill voids, penetrate between unwetted fibers, etc.) favors the use of a high temperature pressing scheme. In contrast, the thermal stability of the materials may favor moderate temperature usage. Therefore, an optimum will exist in which adequate resin flow is manifested during consolidation (i.e., good composite quality) and thermal degradation of the constituents is kept at a minimum.

Time will also be expected to have a similar effect, given that resin flow requires a finite time frame. A high amount of wetting requires an adequate residence time within the press, while the prevention of thermal degradation demands a minimal amount of time in melt consolidation.

Pressure also affects fiber-matrix wetting, given that it is a major driving force in determining resin flow. In a study by Bafna and Baird [1991], carbon fiber tows were consolidated with polyphenylene sulphide (PPS) films to make prepregs. These composite prepregs were manufactured by hot pressing layers of carbon fiber tows sandwiched by PPS films. They were pressed at varying pressures and the resulting composite quality was assessed using optical microscopy. Composites prepared using low pressure (0.35 MPa) were found to contain large areas of excess polymer as well as many void spaces. The higher consolidation pressures (5.5 – 10.8 MPa) yielded samples in which the separate fiber tows were indistinguishable and the polymer matrix was found to penetrate almost all of the gaps within the sample. The conclusion drawn from this data is that high pressure (up to a limit) significantly improves the matrix penetration and consolidation.

A subtle point to note is that the materials in the previous paragraph were prepared by *melt consolidation using film stacking only*, as opposed to *solution prepregging followed by melt consolidation*. The main difference between the melt consolidation process in these two different routes of composite preparation is that the resin flow path is theoretically much shorter for a high quality solution prepregged material. This is because the prepregging process goal is to create as high fiber dispersion and uniformity as possible *before* melt consolidation. Melt consolidation therefore, in the solution prepregging case, is only needed to join plies together and to smooth out any non-uniformities within the prepregs. This is evident from a finding in the study by Lacroix *et al.* [1998]. Regarding their polyethylene composites, they found that a high matrix viscosity during melt consolidation was not a problem in manufacturing, due to the negligible shortness of the flow paths of the matrix in the solution impregnated material. This implies that less severe hot-pressing conditions (as contrasted with film stacking) can be used with solution prepregged fiber tapes and still result in a high-quality composite product.

In a study by Hou *et al*., the effect of compression molding conditions on the quality of carbon fiber reinforced polyetherimide was investigated [1998]. Solvent prepregged carbon fiber fabric reinforced polyetherimide was sandwiched between two polyimide films and consolidated isothermally at different impregnation pressures (0.5 - 4.0 MPa) and residence times (5 - 30 minutes). The quality of the resulting composites was then examined using three point bending tests, optical microscopy of cross sections and void volume analysis using density measurements. The void volume was found to significantly decrease with the increase of either press pressure or residence time during consolidation. Low processing temperatures resulting in high matrix melt viscosity were found to obstruct the impregnation of the reinforcing fabric. Laminates with high void content exhibited a low initial slope in the stress-strain curve during bending. The flexural modulus was found to be negatively correlated with void content.

A suitable approach to observing the effect of input variables such as time, pressure and temperature on output variables such as composite quality is design of experiments [Schmidt and Launsby, 1993]. A designed experiment is typically much more efficient at collecting necessary data to understand a process than an experiment in which one variable is manipulated at a time. This results in a shortened product development time as well as reduced cost. In short, experimental designs are used as: (1) the most effective method for identifying key input variables; (2) the most efficient way to gain an understanding of the relationship between input variables and responses; (3) a method for building a mathematical model which relates input and output variables; and (4) a means to determine optimal settings [Schmidt and Launsby, 1993]. The Box-Behnken designed experiment is particularly useful in modeling processes with 3-level (i.e. pressure 1, pressure 2, pressure 3) quantitative variables (i.e., time, temperature, pressure).

Statistically designed experiments were used in a study by Simmons to determine the effect of mold parameters on the consolidation of propylene/glass fiber composites [1993]. The influence of molding pressure, temperature and dwell time on composite mechanical properties was examined. Mold pressure was varied from 84.5 to 2111 kPa, temperature from 150 to 200 °C and time from 2 to 15 minutes. Measuring interlaminar shear tested the degree of consolidation. Void volume was also measured. Laminates fabricated at low pressure were found to retain high mechanical properties when a high enough temperature was used. In most cases, residence time was found to be an insignificant factor during pressing.

Another thermoplastic composite consolidation study using designed experiments was that of Vovor *et al*. [1994]. Polycarbonate/glass fiber and polypropylene/glass fiber composite systems were studied. The time was varied from ca. 4 to 55 minutes, pressure was varied from ca. 0.1 to 0.85 MPa and temperature was varied from 175 to 225 °C. Short beam shear tests were used to measure the extent of consolidation between the individual laminates. Processing temperature was found to be the most important factor in consolidation. Interactions between temperature and time were also found to be significant.

1.5 Fiber-Matrix Adhesion.

Once the manufacturing process has successfully achieved a uniform dispersion of matrix material around the reinforcing filaments, the fiber-matrix surface interaction must be considered. Fiber-matrix adhesion is widely considered a necessary condition to ensure good composite mechanical properties [Drzal and Madhukar, 1993]. If there is no adhesion between the two, the composite will respond as if it were the bulk matrix material with voids retaining the shape of the included fibers (at low strains). At higher strains, Poisson's effect may bring about mechanical friction forces between the fiber and matrix phase, thus causing the fibers to bring about a greater influence in material properties.

Three general theories can be used to describe the adhesive interaction between two surfaces [Gent and Hamed, 1983]: (1) mechanical interlocking; (2) interdiffusion; and (3) adsorption and surface reaction.

1.5.0 Adhesion by Mechanical Interlocking.

This mechanism of adhesion occurs when a porous or roughly surfaced substrate is brought into contact with a surface that is able to flow and fill the projections of the rough surface. Once the surfaces fully solidify, a mechanically interlocked bond is created. Even if the thermodynamics of surface interaction are not favorable, relatively strong bonds can be created in this manner [Gent and Hamed, 1983]. Mechanical interlocking can be expected to play a role in the joining of porous materials, i.e., wood, paper and textiles. Surface roughening by techniques such as etching can also improve mechanical interlocking in such materials such as metals and plastics.

1.5.1 Adhesion by Interdiffusion.

When the thermodynamics are favorable, it may be possible for molecules of one surface to diffuse into the bulk of another surface and set up an interphase. This interphase represents the elimination of the joining surface and replaces it with a relatively smooth gradient from one bulk material to the other. Depending on the affinity of the molecules toward each other, the interphase may be thin (50 - 100 nanometers) as is the case of most polymers or relatively thick (10 micrometers) [Gent and Hamed, 1983]. Adhesion by interdiffusion can be seen as mechanical interlocking on a molecular scale. This mechanism of adhesion is applicable to materials whose molecules possess a high degree of mobility as well as affinity toward the opposing molecules.

1.5.2 Adhesion by Adsorption and Surface Reaction.

Adhesion by adsorption and surface reaction proceed by the chemical attraction of specific sites by both of the surfaces to be joined [Gent and Hamed, 1983]. These are frequently due to van der Waals forces, ionic interactions, or covalent interactions. In this type of adhesive interaction, the wettability of one surface by a liquid is particularly important - namely, the surface energy of the solid, the surface tension of the liquid and the viscous behavior of the liquid. Wetting of a solid by a liquid is a precursor to adhesion; however, it is not an sufficient condition in forming a strong adhesive joint.

Adhesion between two substrates by adsorption typically requires the wetting fluid to have surface tension less then the critical surface tension of the solid [Schonhorn, 1981]. The critical surface tension of a solid is the tension at which any liquid possessing a lower surface tension will effectively spread and wet the solid substrate (thermodynamic spreading). A liquid with a higher surface tension will form a finite contact angle with the substrate and will not wet the solid surface effectively. The work of adhesion (W_A) for a liquid wetting a solid is given in the following equation:

$$W_A = 2\left(\gamma_S^d \gamma_L^d\right)^{1/2} + 2\left(\gamma_S^p \gamma_L^p\right)^{1/2} \tag{1.2}$$

where: γ= surface tension
subscripts S, L = solid, liquid
superscripts d, p = dispersive, polar contributions to surface tension

In addition to the thermodynamic requirement of compatible surface tensions, the viscosity of the spreading liquid also plays a role in wetting (spreading kinetics). With low molecular weight liquids this is usually not a governing factor, but it increases in importance regarding the use of polymer melts as the wetting liquid. A high viscosity melt could indeed have a lower surface tension then the critical surface tension of a solid, but it must also be given sufficient time to wet-out the solid surface. This can typically be overcome by high residence times at the melt processing temperature and/or increasing the processing temperature.

The interaction between molten thermoplastics and fiber surfaces was examined in a study by Zaborskaya *et al*. [1995]. Various thermoplastic powders such as polysulphone and polyethyleneterephthalate were electrostatically deposited on carbon, glass and organic fillers (poly-*n*-phenyleneterephthalamide). After heat treatment, the fibers were cooled and the contact angles were observed using microscopy. The polymer particle size was found to influence the kinetics of spreading. Smaller drops reached equilibrium contact angles at faster times, while larger particles were observed to never reach equilibrium within the time frame studied. Smaller particles were observed to possess smaller contact angles with the solid surface. The molecular weight of the thermoplastics also affected the kinetics of wetting, as evidenced by higher interlaminar shear strengths of composites made from the materials under study. Maximum strengths of laminated plastics were obtained with polymers that possess excellent melt flow characteristics.

Adhesion in thermoplastic composite systems is usually enhanced using fiber surface treatments. Itoi and Yamada studied the effect of carbon fiber surface modification by oxidation on adhesion with polyethernitrile [1992]. Nitric acid and hydrogen peroxide were used as oxidation agents. Treated fibers were powder impregnated by the polyethernitrile after which unidirectional laminates were obtained. Improvements in interfacial adhesion were monitored using interlaminar shear strength (ILSS) and transverse flexural strength. Interfacial bonding quality improvements were noted in both cases. Both ILSS and transverse flexure strength increased two-fold with fiber treatment. Microscopic examination of fracture surfaces showed excellent bonding after fiber treatment.

Carbon fiber interfaces with thermoplastics were also studied by Chang *et al*. [1994]. Electrochemical treatments as well as the addition of unreacted epoxy sizing were used to alter the interface in the formation of composite laminates. Both fiber treatments were found to increase the transverse and shear strengths by more than 50 % over that of untreated fiber. Furthermore, scanning electron microscopy of fracture surfaces revealed the matrix material had a higher tendency to remain on the fiber surfaces of treated fiber composites.

Metalation treatments were applied to the surface of Kevlar fibers for use in a poly(methyl methacrylate) matrix [Chen *et al*., 1988]. Allylation, ethoxycarbonylmethylation and carboxymethylation were all used to modify the fiber surface. The single fiber pull out test was then used to assess interfacial adhesion with the polymer matrix. Smaller critical immersion lengths were noted for all fiber treatments over that of untreated fiber, indicative of higher interfacial shear stresses. Carboxymethylation treatment was found to increase the interfacial shear stress the most over that of other fiber surface treatments. In general, the introduction of polar surface groups onto the Kevlar fiber was found to increase fiber/matrix adhesion.

1.6 Biobased Thermoplastic Composites.

During recent years, the awareness of potential problems has grown regarding the use of conventional petroleum-based polymer products. Of particular concerns are both the non-renewable nature of petrochemical feedstock as well as the problems associated with waste disposal at the end of the product life cycle. Therefore, alternative polymer materials are being sought in an effort to address these problems. A largely underutilized source of polymeric materials is woody biomass. Trees, which contain cellulose (ca. 50%), hemicelluloses and lignin, represent an abundant source for renewable polymers that possess high degradability. Cellulose in particular represents the most abundant natural polymer in existence.

Lignocellulosic fillers and fibers have recently been investigated in synthetic polymer composite systems. Their potential to enhance the mechanical properties over a neat polymer matrix (particularly impact toughness and stiffness) and to reduce the final cost of the material as well as increase the biodegradable component content within the material makes the use of biobased polymers very attractive. Cellulose-containing fibers, such as bamboo, henequen and wood flour/ fibers, have been studied in the context of their reinforcing properties within conventional thermoplastic materials. Various matrix materials combined with natural fibers include poly(propylene) [Chen *et al*., 1998; Takase and Shiraishi, 1989; Oksman and Clemons, 1998; Klason *et al*., 1984; Dalvag *et al*., 1985], various poly(ethylene)s [Raj *et al*., 1989; Herrera-Franco and Aguilar-Vega, 1997] and poly(methyl methacrylate) [Maldas *et al*., 1989].

A common problem associated with these composite systems is poor interfacial adhesion between the hydrophobic matrix material and the hydrophilic filler, resulting in poor mechanical properties in the final material. This is often addressed by the use of adhesion-promoting agents such as a coupling agent, or a fiber-surface modifying treatment. Another common problem associated with the use of incompatible materials within short-fiber composites is poor fiber dispersion within the matrix. Additives, which compatibilize the different solid phases within the composite, have been found to contribute to the development of a more even fiber distribution within the final material.

Among biopolymeric materials, cellulose and cellulose derivatives enjoy widespread use and remain the single largest biopolymer. In multiphase polymer materials, cellulose may find application in both polymeric blends [Masson and St. John Manley, 1992] and as fibers in reinforced polymeric composites.

Studies on the role of cellulose-fiber reinforcement abound in the literature. Many types of surface modifiers have been employed in order to improve the interfacial adhesion between cellulose and the matrix material. Cellulase-enzyme treatment has been used in modifying the surface characteristics of cellulose fibers for application in low-density poly(ethylene) [Kim *et al*., 1997], as well as mechanical treatments to increase the aspect ratio of the cellulose fibers for use in poly(propylene) [Klason *et al*., 1989].

Rubberwood fibers and powder were treated with two types of coupling agents in an attempt to enhance interfacial adhesion with high-density polyethylene [Rozman et al., 1998]. Agglomeration of untreated fibers within the thermoplastic matrix resulted in inferior mechanical properties of the composite system. The coupling agent 3-(trimethoxysilyl) propyl methacrylate significantly improved the modulus of elasticity and impact strength of the rubberwood fiber composites. The 3-aminopropyltriethoxysilane coupling agent reduced the tensile modulus but increased the elongation at break for both the powder and fiber filled polyethylene composites.

A widely studied method of compatibilizing cellulose with a thermoplastic matrix is the use of polymer grafting techniques. In a study by Beshay and Hoa [1990], silane coupling agents were grafted onto the surface of cellulose fibers to increase adhesion in poly(vinyl chloride) (PVC) and poly(styrene) (PS). It was found that untreated fiber filled materials decreased in tensile strength, due to poor interfacial bonding. By using grafted fibers, tensile strength increases were obtained in both PS and PVC, with increases ranging from 13 to 69% over that of the neat resin (for fiber contents ranging from 10 to 30% w/w).

In a series of studies by Felix and Gatenholm [Felix and Gatenholm, 1990; 1991; 1993], modified cellulose fibers were used as a reinforcing agent in poly(propylene) (PP). Coupling agents, polymer grafts and heat treatments were all used to modify the surface character of the cellulose fibers. Specifically, acid/ base interactions were tailored in order to promote an increase in the fiber/matrix adhesion. It was found that heat and chloro-silane treatments increased the acidity of the fiber surface, while amino-silane treatment increased the basicity (observed using inverse gas chromatographic methods). Composite materials were then produced and analyzed using dynamic mechanical methods as well as studying stress-strain relationships. It was found that acid/ base forces have an influence on dynamic mechanical parameters (such as storage and loss moduli and tanδ) and that strengthening the acid/ base interactions between the reinforcement and the matrix becomes apparent in elastic modulus increases. Furthermore, by using poly(propylene)-malaic anhydride copolymers grafted to the surface of cellulose fibers, adhesion with PP was improved, therefore increasing the mechanical properties (such as tensile modulus) over neat PP.

Joly *et al.* has also studied the use of grafting techniques in order to increase interfacial adhesion between cellulose fibers and PP [1996]. PP segments were grafted to the fiber surface via an ester bond, with the free segment left to co-crystallize and otherwise entangle with the bulk PP matrix. The second treatment studied was the grafting of a small aliphatic side-chain (to decrease hydrophilic character of the fiber) to the fiber surface using a urethane bond. These two different treatments were found to affect the crack initiation and propagation properties within the composite material. The grafting of the small aliphatic chains was found to increase the rupture propagation strength in the composite without modifying the crack initiation properties. The aliphatic chains are believed to exert a compatibilizing effect. The grafting of PP segments to the cellulose fiber surface was also found to increase compatibility as well as increase the modulus of the interphase between the fibers and the matrix. The rupture initiation strength of the composite was found to increase and other related adhesion properties were also found to increase.

The use of coupling agents has also been investigated to improve interfacial adhesion between cellulose fibers and poly(styrene) [Maldas *et al*., 1989]. It was found that PS-precoated fibers treated with isocyanate was a superior fiber treatment over that of conventional silane coupling agent usage. Isocyanate is thought to participate in the formation of covalent bonds between cellulose and PS, while the silane coupling agents produce weaker (by comparison) hydrogen bond and VdW interactions. This was evident in mechanical property evaluation: silane treatments decreased or only slightly increased properties such as tensile strength, elongation, energy at the maximum point, as well as the tensile modulus at 0.1% strain, whereas isocyanate treated fiber composites with fiber precoat exhibited large increases in these properties over the neat resin.

Direct grafting of poly(ethylene) (PE) onto cellulose fibers using dicumyl- and benzoyl-peroxide has been studied to improve the adhesion between cellulose fibers and PE [Saphieha *et al*., 1990]. The mechanical properties used to evaluate interfacial adhesion were tensile yield stress and elastic modulus. Mechanical property increases were attributed to peroxide induced grafting, with the grafting reactions terminating at the point of 100% fiber surface coverage by PE grafts. A critical peroxide concentration was established as the concentration above which the grafting reaction is terminated.

Kraft pulp was subjected to stearic acid in order to enhance fiber-matrix composite dispersion in polypropylene [Raj and Kokta, 1989]. Dispersion was observed by measuring the size and number of agglomerates within a compression molded sheet. The number of fiber aggregates as well as their size decreased with stearic acid treatment. Increases in stearic acid concentration within the fiber above 10 % resulted in only a marginal decrease in the number of aggregates. Stearic acid treatment also lowered the water retention within treated pulp fibers.

Continuous, regenerated cellulose fibers have been used as reinforcement in thermoplastic poly(3-hydroxybutyrate)-co-poly(3-hydroxyvalerate) (PHB/V) [Bourban *et al*., 1997]. The matrix polymer was applied in powder form using a fluidized bed. Composites with fiber volume contents of up to 30 volume percent were produced and characterized. Tensile properties included ultimate strength values ranging from 128 to 278 MPa, with a modulus ranging from 6 to 11 GPa. However, poor interfacial adhesion was found to be a drawback in this biobased composite system.

The incorporation of the biobased polymers with synthetic thermoplastic materials does not create a completely biodegradable material. Biobased fiber/ biobased matrix systems have received relatively little attention as of late. Examples of complete biobased polymer composite systems studied include the use of natural fibers as reinforcing agents in natural polymer matrices such as natural rubber and poly(hydroxy-butyrate) [Geethamma *et al*., 1997; Avella *et al*., 1993]. By exercising judicious selection methods, lignocellulosic materials (or thermoplastic derivatives) serving as both fiber and matrix components can enjoy favorable interfacial interactions.

A common surface modification method for lignocellulosic fibers is surface esterification. Reducing the polarity of wood fibers and flakes using this method has been shown to increase dimensional stability to moisture and decrease susceptibility to degradation by biological organisms, heat and ultraviolet radiation [Rowell *et al*., 1986; 1990; 1993; 1995]. In whole wood fibers, the majority of the esterification takes place in the lignin and hemicellulose, while cellulose displays a low reactivity to acetic anhydride [Ramsden and Blake, 1997; Hill *et al*., 1998; Rowell *et al*., 1994]. Other biobased fibers subjected to acetylation include jute and sisal [Rana *et al*., 1997; Chand et al., 1989]. Jute fibers were subjected to acetylation with and without cosolvent (pyridine). Thermal stability by thermogravimetric analysis (TGA) was found to increase. Acetylated sisal fibers showed decreased equilibrium moisture content; however, they also showed a decrease in tensile strength.

Acetylated fibers have also been used in the manufacture of polymer composites. Devi, *et al*. produced acetylated pineapple leaf fiber reinforced polyester composites [1997]. Both flexural as well as tensile properties increased significantly over neat matrix with the inclusion of modified fiber. Laminates of acetylated fibers and polyolefins have also been investigated [Westin and Simonson, 1992]. A decrease in moisture uptake of laminates made from modified fibers improved the retention of flexural modulus under wet conditions. In a recent study by Glasser *et al.*, thermoplastic composite materials with CAB as matrix were produced using discontinuous water extracted steam exploded fibers, alkali extracted fibers, untreated oat fibers and acetylated fibers [1999]. The acetylated lignocellulosic fibers were found to have considerable adhesion to a thermoplastic cellulose ester over that of chemically unmodified fiber, as evidenced by a decrease in the fiber pull-out phenomena on composite fiber fracture surfaces and an increase in tensile modulus with the addition of fiber according to the rule of mixtures model.

1.7. Objectives.

A new biobased composite system is currently under investigation at the Biobased Materials/ Recycling Center of Virginia Tech. This system is comprised of CAB serving as a thermoplastic matrix material and high modulus regenerated cellulose fibers as reinforcement. This material is expected to find applications as indoor structural panels such as in cabinets or doors, in sporting goods and in transportation-related articles. Improvements over conventional wood composites and veneers can include a reduction in weight and increases in certain mechanical properties such as impact toughness, while still retaining degradability and not changing the source of the material (renewable).

Work completed prior to this study involved the screening of composite manufacturing techniques, including solution prepregging of fiber tows, suspension powder prepregging and film stacking [Glasser and Davis, 1999]. Solution prepregged composites were found to be limited by void formation due to entrapped solvent. Film-stack prepared composites were found to be limited by the high melt viscosity of the matrix material. All composites revealed extensive interfacial delamination and fiber pullout. The surface of untreated cellulose fibers appeared to physically separate from the matrix during fiber-direction-tensile testing. This can be indicative of weak fiber - matrix adhesion. Therefore, fiber surface acetylation will be pursued as a method with which the interfacial adhesion can possibly be improved. Composites containing both acetylated and unacetylated fibers will be produced by solution coating and tested in tensile mode. Microscopy will be used to examine the resulting fracture surfaces. At the conclusion of this first section, the nature of adhesion between cellulose and CAB shall be elucidated as well as a potential method with which to improve it.

After investigative work is completed regarding the nature of the interface between cellulose and CAB, a systematic evaluation of the hot pressing conditions will be undertaken in order to determine what conditions (i.e., temperature, pressure, and press time) are optimal in terms of manufacturing a composite having minimal void content as well as high interlaminar shear properties. Press conditions will be systematically varied using a design of experiments scheme while monitoring interlaminar shear strength, void and fiber volume content within final composites, as well as tensile behavior of the manufactured materials. This section attempts to identify manufacturing conditions at which composites are produced which display an optimal quality of consolidation (hereby measured using interlaminar shear strength and void volume content).

CHAPTER 2.

Theoretical: A Diffusing Reaction through Simultaneous Mass Transfer and Reaction Modeling.

2.0 Abstract.

The diffusing reaction of hydroxyl substituents within a cellulose fiber by gaseous acetic anhydride was modeled using mass transfer and reaction rate theory. The finite element method was then employed to formulate a numerical solution for the resulting system of partial differential equations.

The finite element model was evaluated for accuracy by predicting solutions for diffusion alone and reaction alone. Good agreement was found with the series solution for Fickian diffusion as well as the analytical solution for the reaction term.

However, the model has not been fitted to the experimental system due to the inability to accurately measure concentration distributions within the system. Before further work can continue on model refinement, experimental observations must be made in order to determine actual rate and diffusion parameters.

2.1 Introduction.

Fiber reinforced polymer composites frequently suffer from lack of fiber - matrix adhesion. This is frequently addressed by chemically modifying the fiber surface in an attempt to bring about greater adhesion with the matrix material. Modification of the fiber surface is desired for the enhancement of surface properties, while the bulk reinforcement chemical composition should remain unchanged to preserve fiber strength [Canche-Escamilla *et al*., 1999; Chand *et al*., 1989].

Experiments taking place at the Biobased Materials / Recycling Center at Virginia Tech deal with cellulose fiber reinforced cellulose acetate butyrate (matrix). In order to enhance fiber - matrix adhesion in this system, acetylation of the cellulose fiber surface hydroxyl groups using gaseous acetic anhydride has been investigated. The reaction proceeds by the combination of equal amounts of anhydride and cellulose hydroxyl groups to produce ester (acetate) groups.

Assumptions used in developing this initial model include a constant diffusion coefficient, uniform fiber morphology (i.e., all regions are regarded as uniformly amorphous), as well as a constant volume and density of the reacting fiber. All of these assumptions were taken in order to simplify the numerical solution as well as a general lack of accurate data regarding fiber morphology, relative cellulose - cellulose acetate densities and the diffusion coefficient variance with penetrant concentration.

2.2 Defining the Problem.

A finite cylinder initially has a given concentration of ‘a’ groups ([a = hydroxyl groups]) distributed evenly throughout its volume. At zero time (t = 0), a diffusing reactant ‘b’ ([b = acetic anhydride groups]) enters into the cylinder from all sides and reacts with ‘a’ to form ‘c’ ([c = acetate ester groups]). In this case, ‘a’ and ‘c’ are solid, immobile reactants and products, respectively, while ‘b’ is the diffusing reactant.

This 3-dimensional body will be modeled as a 2-dimensional plane (radial - height plane) due to symmetry. Furthermore, since there are also axes of symmetry along the middle of the body and half way through the height, only the upper right quarter of the plane will be simulated (Figure 2.0.).

2.3 Formulating the Governing Equations.

Each of the chemical species can be modeled using a partial differential equation with respect to *r-z* space (two dimensional) and time containing a reaction rate term and a diffusion term for the diffusing species ‘b.’ In this case, the reaction rate will be assumed to be first order in each of the reactants and the diffusion will proceed according to binary Fickian diffusion with a constant diffusion coefficient. 'a'-'c' notation will be used in the equation labels as denoting 'a'-'c' species governing equations, respectively.

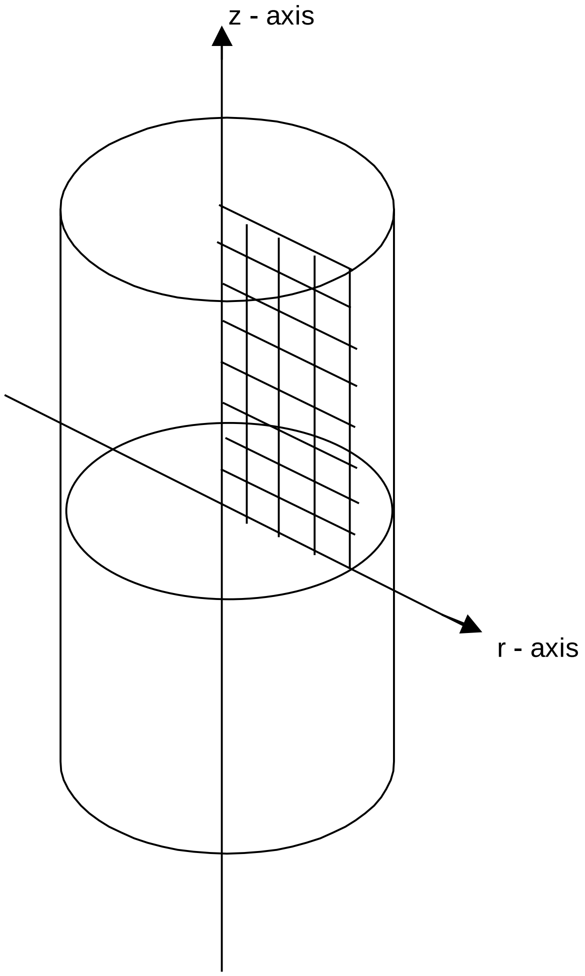

Figure 2.0 Experimental Volume and Theoretical Model Area.

$$\frac{\partial[a]}{\partial t} = -k[a][b] \tag{2.0.a}$$

$$\frac{\partial[b]}{\partial t} = D\left[\frac{\partial^2[b]}{\partial z^2} + \frac{\partial^2[b]}{\partial r^2} + \frac{1}{r}\frac{\partial[b]}{\partial r}\right] - k[a][b] \tag{2.0.b}$$

$$\frac{\partial[c]}{\partial t} = k[a][b] \tag{2.0.c}$$

where *k* is the reaction rate constant and *D* is the diffusion coefficient for reactant 'b.'

The initial conditions for this problem consist of the following:

$[c] = 0$ for $0 < r <$ a, $0 <$ z $<$ b
$[b] = 0$ for $0 \leq$ r $<$ a, $0 \leq$ z $<$ b

$[a] = i_a$ = constant for $0 \le r \le a$, $0 \le z \le b$

where ‘a’ is the radius of the cylinder and ‘b’ is half the height of the cylinder, and the following boundary conditions apply:

@ $r = a$, $[b] = i_b$ = constant
@ $z = b$, $[b] = i_b$ = constant
@ $r = 0$, $\partial[b]/\partial r = 0$
@ $z = 0$, $\partial[b]/\partial z = 0$

2.4 Formulating the Problem Statement.

Rearranging Eq. (2.0.a-c), we obtain the following:

$$\frac{\partial[a]}{\partial t} + k[a][b] = 0 \qquad (2.1.a)$$

$$\frac{\partial[b]}{\partial t} - D\left[\frac{\partial^2[b]}{\partial z^2} + \frac{\partial^2[b]}{\partial r^2} + \frac{1}{r}\frac{\partial[b]}{\partial r}\right] + k[a][b] = 0 \qquad (2.1.b)$$

$$\frac{\partial[c]}{\partial t} - k[a][b] = 0 \qquad (2.1.c)$$

To obtain the Galerkin formulation for the partial differential equation (2.1.b), we first multiply it by a test function V and integrate over the problem domain Ω ($\Omega = \{-a \le r \le a, -b \le z \le b\}$). The problem now becomes the following:

Find $[i] \in H^1_E$, $i = a, b, c$ $\forall v \in H^1_0$ where the space H^1_0 is the space in which all functions and their first derivatives are square integrable and take on the value of zero at the domain boundary and the space H^1_E is the space in which all functions are square integrable and satisfy the essential boundary conditions (Eqs. (2.1.a) and (2.1.c) will be dealt with later):

$$\frac{\partial[a]}{\partial t} + k[a][b] = 0 \qquad (2.2.a)$$

$$\iint_\Omega v\left(\frac{\partial[b]}{\partial t} - D\left[\frac{\partial^2[b]}{\partial z^2} + \frac{\partial^2[b]}{\partial r^2} + \frac{1}{r}\frac{\partial[b]}{\partial r}\right] + k[a][b]\right)drdz = 0 \qquad (2.2.b)$$

$$\frac{\partial[c]}{\partial t} - k[a][b] = 0 \qquad (2.2.c)$$

Upon expanding Eq. (2.2) for the 'b' equation, we obtain:

$$\iint_{\Omega} v\left(\frac{\partial[b]}{\partial t}\right)drdz - D\iint_{\Omega} v\left(\frac{\partial^2[b]}{\partial z^2}+\frac{\partial^2[b]}{\partial r^2}\right)drdz$$
$$- D\iint_{\Omega} v\left(\frac{1}{r}\frac{\partial[b]}{\partial r}\right)drdz + k\iint_{\Omega} v\ ([a][b])drdz = 0 \qquad (2.3.b.0)$$

By using Green's Theorem (Divergence Theorem), the second integral term in Eq. (2.3.b.1) can be expanded to produce the following governing equation for species 'b':

$$\iint_{\Omega} v\left(\frac{\partial[b]}{\partial t}\right)drdz + D\iint_{\Omega}\left(\frac{\partial v}{\partial r}+\frac{\partial v}{\partial z}\right)\bullet\left(\frac{\partial[b]}{\partial r}+\frac{\partial[b]}{\partial z}\right)drdz$$
$$- D\int_{\partial\Omega} v\left(\frac{\partial[b]}{\partial r}+\frac{\partial[b]}{\partial z}\right)\bullet nds - D\iint_{\Omega} v\left(\frac{1}{r}\frac{\partial[b]}{\partial r}\right)drdz + k\iint_{\Omega} v\ ([a][b])drdz = 0 \qquad (2.3.b.1)$$

Because $v \in H^1{}_0$, the surface integral in Eq. (2.3.b.2) vanishes, resulting in Eq. (2.3.b.3):

$$\iint_{\Omega} v\left(\frac{\partial[b]}{\partial t}\right)drdz + D\iint_{\Omega}\left(\frac{\partial v}{\partial r}+\frac{\partial v}{\partial z}\right)\bullet\left(\frac{\partial[b]}{\partial r}+\frac{\partial[b]}{\partial z}\right)drdz$$
$$- D\iint_{\Omega} v\left(\frac{1}{r}\frac{\partial[b]}{\partial r}\right)drdz + k\iint_{\Omega} v\ ([a][b])drdz = 0 \qquad (2.3.b.2)$$

Now we are ready to discretize the domain as well as introduce the interpolants. We will proceed by dividing the two-dimensional domain into a N_r X N_z uniform quadrilateral mesh, with N_r denoting the number of elements along the r-axis and N_z denoting the number of elements along the z-axis. The total number of elements is N_Δ, which is the product of N_r and N_z. We will introduce the following Lagrangian interpolants for the real functions denoting the concentrations of species as a function of space and time, as well as the test function v:

$$[i] \approx [I] = \sum_{i=1}^{4} c_{i,I}\phi_{i,I}$$
$$v \approx V = \sum_{j=1}^{4} d_j\phi_j \qquad (2.4)$$

The interpolants used are simple first order bilinear shape functions that are unity at the vertices of the quadrilateral element while the coefficients c and d represent the finite element solution at the specified nodes (discussed in the later section *Defining the Basis Functions*).

Discretizing Eqs. (2.2.a), (2.3.b.2) and (2.2.c), we obtain Eqs. (2.5.a), (2.5.b) and (2.5.c), respectively:

$$\left(\left(\frac{\partial[A]}{\partial t}\right)+k([A][B])\right)=0 \tag{2.5.a}$$

$$\sum_{e=1}^{N_\Delta}\left(\begin{array}{l}\displaystyle\iint_{\Omega_e}V\left(\frac{\partial[B]}{\partial t}\right)drdz+D\iint_{\Omega_e}\left(\frac{\partial V}{\partial r}\frac{\partial[B]}{\partial r}+\frac{\partial V}{\partial z}\frac{\partial[B]}{dz}\right)drdz\\ \displaystyle -D\iint_{\Omega_e}V\left(\frac{1}{r}\frac{\partial[B]}{\partial r}\right)drdz+k\iint_{\Omega_e}V([A][B])drdz\end{array}\right)=0 \tag{2.5.b}$$

$$\left(\left(\frac{\partial[C]}{\partial t}\right)-k([A][B])\right)=0 \tag{2.5.c}$$

where the integral space Ω_e is the real domain element.

2.5 Generating the Mesh.

The N_r X N_z quadrilateral mesh will first be plotted on a square with the ordinate being the ξ-axis and the abscissa being the η-axis. The coordinates of this square in ξ-η space, starting from the lower left-hand corner and moving counter clockwise, are (0,0), (1,0), (1,1) and (0,1). The mesh intersection points represent the nodes of the mesh as well as the vertices of the quadrilateral elements. Once the nodal coordinates are obtained in ξ-η space, we can employ *blend mapping* in order to obtain the nodal coordinates in real space (r-z space). An example for a 4 X 4 mesh is given in Figure 2.1.

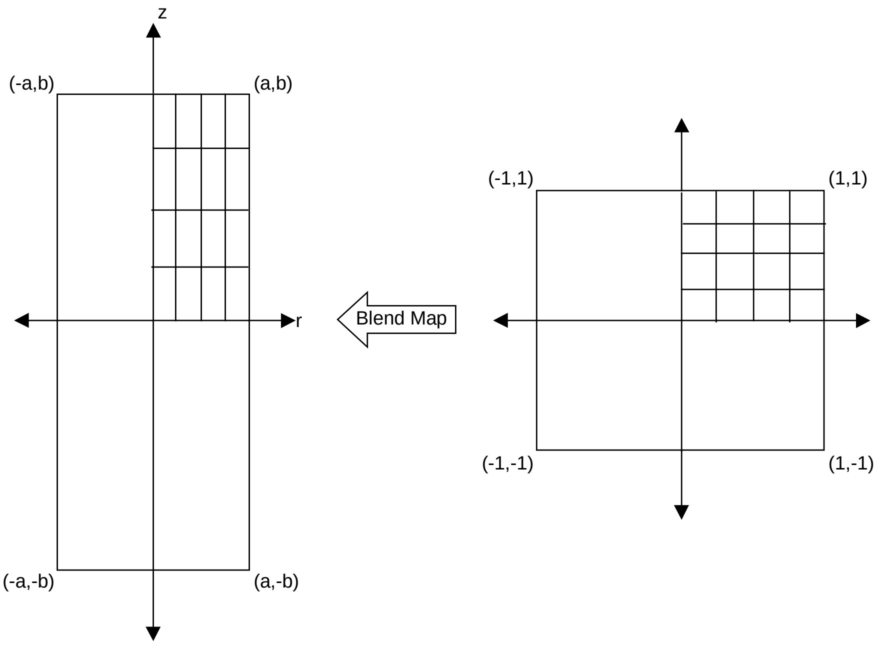

Figure 2.1 Blend Map Example using a 4X4 Mesh.

The real space element vertex coordinates can be expressed in terms of ξ and η by the following equations:

$$r(\xi,\eta) = N_1(\xi)r_4(\eta) + N_2(\xi)r_2(\eta) + N_1(\eta)r_1(\xi) + N_2(\eta)r_3(\xi) - \sum_{i,j=1}^{2} N_i(\xi)N_j(\eta)\left(r_{i,j}\right) \quad (2.6.a)$$

$$z(\xi,\eta) = N_1(\xi)z_4(\eta) + N_2(\xi)z_2(\eta) + N_1(\eta)z_1(\xi) + N_2(\eta)z_3(\xi) - \sum_{i,j=1}^{2} N_i(\xi)N_j(\eta)\left(z_{i,j}\right) \quad (2.6.b)$$

in which the last parentheses contains the vertex point coordinate for vertex *i,j* in real space and the subscripts *1-4* on the functions *r(ξ or η)* and *z(ξ or η)* denote the particular edge of the domain, starting with number *1* for the bottom edge and numbering consecutively going counter clockwise.

The functions r_1-r_4 are given as follows:

$$\begin{aligned} r_1(\xi) &= a\xi \\ r_2(\eta) &= a \\ r_3(\xi) &= a\xi \\ r_4(\eta) &= 0 \end{aligned} \quad (2.7.a)$$

where '*a*' in this case is the radius of the cylinder.

The corresponding functions in the z direction are next:

$$\begin{aligned} z_1(\xi) &= 0 \\ z_2(\eta) &= b\eta \\ z_3(\xi) &= b \\ z_4(\eta) &= b\eta \end{aligned} \quad (2.7.b)$$

Lastly, the *N* shape functions will be defined (same for (2.6.a) and (2.6.b)):

$$\begin{aligned} N_1(\xi) &= \frac{\xi_2 - \xi}{\xi_2 - \xi_1} = 1 - \xi \\ N_1(\eta) &= \frac{\eta_2 - \eta}{\eta_2 - \eta_1} = 1 - \eta \\ N_2(\xi) &= \frac{\xi - \xi_1}{\xi_2 - \xi_1} = \xi \\ N_2(\eta) &= \frac{\eta - \eta_1}{\eta_2 - \eta_1} = \eta \end{aligned} \quad (2.7.c)$$

Now, by substituting the expressions in Eq. (2.7) into Eq. (2.6), a quadrilateral mesh containing N_Δ elements is generated in the real domain. The following continuous equations relate *r* coordinates to ξ and *z* coordinates to η:

$$\begin{aligned} r(\xi,\eta) &= a\xi \\ z(\xi,\eta) &= b\eta \end{aligned} \tag{2.8}$$

2.6 Defining the Basis Functions.

We will define our finite element basis on the canonical element (Ω_0). This element represents a square in ξ-η space, with vertices of (0,0), (1,0), (1,1) and (0,1). The interpolants in Eq. (2.4) can now be expanded in the following manner using piecewise defined linear shape functions for the vertices:

$$\begin{aligned} [i]_e \approx [I]_e &= \sum_{i=1}^{4} c_{i,I}\phi_{i,I} = \sum_{i,j=1}^{2} c_{i,j}(t) N_{ij}^1(\xi,\eta) \\ v_e \approx V_e &= \sum_{j=1}^{4} d_j\phi_j = \sum_{i,j=1}^{2} d_{i,j}(t) N_{ij}^1(\xi,\eta) \end{aligned} \tag{2.9}$$

where:

$$N_{i,j}^1 = N_i(\xi) N_j(\eta) \tag{2.10}$$

for *i* = 1 to 2

and the functions *N* are defined as the following:

$$\begin{aligned} N_1(\xi) &= \frac{\xi_2-\xi}{\xi_2-\xi_1} = 1-\xi \\ N_1(\eta) &= \frac{\eta_2-\eta}{\eta_2-\eta_1} = 1-\eta \\ N_2(\xi) &= \frac{\xi-\xi_1}{\xi_2-\xi_1} = \xi \\ N_2(\eta) &= \frac{\eta-\eta_1}{\eta_2-\eta_1} = \eta \end{aligned} \tag{2.11}$$

2.7 Transforming the Real Domain into the Canonical Element for the Governing Equations.

Starting with Eqs. (2.5.b), we can change the integration space from the real space element into the canonical element by multiplying each integration argument by the determinant of the Jacobian of the transformation:

$$\sum_{e=1}^{N_\Delta}\left(\begin{array}{l}\displaystyle\iint_{\Omega_0} V\left(\frac{\partial[B]}{\partial t}\right)(\det J_e)d\xi d\eta + D\iint_{\Omega_0}\left(\frac{\partial V}{\partial \xi}\frac{\partial[B]}{\partial \xi}\left(\frac{\partial \xi}{\partial r}\right)^2 + \frac{\partial V}{\partial \eta}\frac{\partial[B]}{d\eta}\left(\frac{\partial \eta}{\partial z}\right)^2\right) \\ \qquad (\det J_e)d\xi d\eta \\ \displaystyle - D\iint_{\Omega_0} V\left(\frac{1}{r(\xi,\eta)}\frac{\partial[B]}{\partial \xi}\frac{\partial \xi}{\partial r}\right)(\det J_e)d\xi d\eta + k\iint_{\Omega_0} V([A][B])(\det J_e)d\xi d\eta\end{array}\right) = 0 \qquad (2.12.b)$$

The integrations are now all performed over the canonical element, Ω_0. The determinant of the Jacobian of the transformation is constant for this case:

$$\det J_e = \det\begin{bmatrix} r_\xi & r_\eta \\ z_\xi & z_\eta \end{bmatrix} = \det\begin{bmatrix} a/N_r & 0 \\ 0 & b/N_z \end{bmatrix} = \frac{ab}{N_r N_z} \qquad (2.13)$$

Now we are ready to define all the variables in Eqs. (2.12.a-c) using Eqs. (2.9), (2.10) and (2.11):

$$[I] = \begin{bmatrix} c_{1,I} \\ c_{2,I} \\ c_{3,I} \\ c_{4,I} \end{bmatrix}\begin{bmatrix} 1-\xi-\eta+\xi\eta & \xi-\xi\eta & \xi\eta & \eta-\xi\eta \end{bmatrix} \qquad (2.14)$$

$$\frac{\partial[I]}{\partial t} = \begin{bmatrix} \dot{c}_{1,I} \\ \dot{c}_{2,I} \\ \dot{c}_{3,I} \\ \dot{c}_{4,I} \end{bmatrix}\begin{bmatrix} 1-\xi-\eta+\xi\eta & \xi-\xi\eta & \xi\eta & \eta-\xi\eta \end{bmatrix} \qquad (2.15)$$

$$\frac{\partial[B]}{\partial \xi} = \begin{bmatrix} c_{1,B} \\ c_{2,B} \\ c_{3,B} \\ c_{4,B} \end{bmatrix}\begin{bmatrix} -1+\eta & 1-\eta & \eta & -\eta \end{bmatrix} \qquad (2.16)$$

$$\frac{\partial[B]}{\partial \eta} = \begin{bmatrix} c_{1,B} \\ c_{2,B} \\ c_{3,B} \\ c_{4,B} \end{bmatrix}\begin{bmatrix} -1+\xi & -\xi & \xi & 1-\xi \end{bmatrix} \qquad (2.17)$$

$$V=\begin{bmatrix} d_1 & d_2 & d_3 & d_4 \end{bmatrix}\begin{bmatrix} 1-\xi-\eta+\xi\eta \\ \xi-\xi\eta \\ \xi\eta \\ \eta-\xi\eta \end{bmatrix} \tag{2.18}$$

$$\frac{\partial V}{\partial \xi}=\begin{bmatrix} d_1 & d_2 & d_3 & d_4 \end{bmatrix}\begin{bmatrix} -1+\eta \\ 1-\eta \\ \eta \\ -\eta \end{bmatrix} \tag{2.19}$$

$$\frac{\partial V}{\partial \eta}=\begin{bmatrix} d_1 & d_2 & d_3 & d_4 \end{bmatrix}\begin{bmatrix} -1+\xi \\ -\xi \\ \xi \\ 1-\xi \end{bmatrix} \tag{2.20}$$

$$\begin{aligned} \left(\frac{\partial \xi}{\partial r}\right)^2 &= \frac{N_r^2}{a^2} \\ \left(\frac{\partial \eta}{\partial z}\right)^2 &= \frac{N_z^2}{b^2} \end{aligned} \tag{2.21}$$

$$r(\xi,\eta)=\frac{a}{N_r}\xi+(\text{int.}=f(e)) \tag{2.22}$$

where *a* is the radius of the cylinder and *int.* is a function of the particular element which one is performing the integrations over.

Upon performing these substitutions as well as integrating, we obtain the problem:

$$\sum_{e=1}^{N_\Delta}\left[\left[\underline{\underline{\alpha}}\bullet\underline{\dot{c}_A}\right]+k\left[\underline{\underline{\alpha}}\bullet\underline{c_A c_B}\right]\right]=0\ \text{(2.23.a)}$$

$$\sum_{e=1}^{N\Delta}\begin{bmatrix} \det J_e\left[\underline{\underline{\beta}}\bullet\underline{\dot{c}_B}\right]+ \\ D\det J_e\,\dfrac{N_r^2}{a^2}\left[\underline{\underline{\chi}}\bullet\underline{c_B}\right]+ \\ D\det J_e\,\dfrac{N_z^2}{b^2}\left[\underline{\underline{\delta}}\bullet\underline{c_B}\right]- \\ D\det J_e\,\dfrac{N_r}{a}\left[\displaystyle\iint_{\Omega_0}\frac{1}{r(\xi,\eta)}\underline{\underline{\varepsilon}}\,d\xi d\eta\bullet\underline{c_B}\right]+ \\ k\det J_e\left[\underline{\underline{\phi}}\bullet\underline{c_A c_B}\right] \end{bmatrix}=0 \tag{2.23.b}$$

And lastly, for species 'C':

$$\sum_{e=1}^{N_\Delta}\left[\left[\underline{\underline{\alpha}}\bullet\underline{\dot{c}_C}\right]-k\left[\underline{\underline{\alpha}}\bullet\underline{c_Ac_B}\right]\right]=0 \qquad (2.23.c)$$

with the following values for the vectors and matrices (in order of appearance):

$$\underline{\dot{c}_A}=\begin{bmatrix}\dot{c}_{1,A}\\ \dot{c}_{2,A}\\ \dot{c}_{3,A}\\ \dot{c}_{4,A}\end{bmatrix}$$

$$\underline{\underline{\alpha}}=\begin{bmatrix}1&0&0&0\\0&1&0&0\\0&0&1&0\\0&0&0&1\end{bmatrix}$$

$$\underline{c_Ac_B}=\begin{bmatrix}c_{1,A}c_{1,B}\\ c_{2,A}c_{2,B}\\ c_{3,A}c_{3,B}\\ c_{4,A}c_{4,B}\end{bmatrix}$$

$$\underline{\dot{c}_B} = \begin{bmatrix} \dot{c}_{1,B} \\ \dot{c}_{2,B} \\ \dot{c}_{3,B} \\ \dot{c}_{4,B} \end{bmatrix}$$

$$\underline{\underline{\beta}} = \begin{bmatrix} 1/9 & 1/18 & 1/36 & 1/18 \\ 1/18 & 1/9 & 1/18 & 1/36 \\ 1/36 & 1/18 & 1/9 & 1/18 \\ 1/18 & 1/36 & 1/18 & 1/9 \end{bmatrix}$$

$$\underline{c_B} = \begin{bmatrix} c_{1,B} \\ c_{2,B} \\ c_{3,B} \\ c_{4,B} \end{bmatrix}$$

$$\underline{\underline{\chi}} = \begin{bmatrix} 1/3 & -1/3 & -1/6 & 1/6 \\ -1/3 & 1/3 & 1/6 & -1/6 \\ -1/6 & 1/6 & 1/3 & -1/3 \\ 1/6 & -1/6 & -1/3 & 1/3 \end{bmatrix}$$

$$\underline{\underline{\delta}} = \begin{bmatrix} 1/3 & 1/6 & -1/6 & -1/3 \\ 1/6 & 1/3 & -1/3 & -1/6 \\ -1/6 & -1/3 & 1/3 & 1/6 \\ -1/3 & -1/6 & 1/6 & 1/3 \end{bmatrix}$$

$$\underline{\underline{\varepsilon}} = \begin{bmatrix} A & -A & B & -B \\ C & -C & D & -D \\ -D & D & E & -E \\ -B & B & F & -F \end{bmatrix}$$

$$\underline{\underline{\phi}} = \begin{bmatrix} 1/16 & 1/48 & 1/144 & 1/48 \\ 1/48 & 1/16 & 1/48 & 1/144 \\ 1/144 & 1/48 & 1/16 & 1/48 \\ 1/48 & 1/144 & 1/48 & 1/16 \end{bmatrix}$$

where the expressions A through F are given by:

$$
\begin{aligned}
&A = -1 + \xi + 2\eta - 2\xi\eta - \eta^2 + \xi\eta^2 \\
&B = \eta - \xi\eta - \eta^2 + \xi\eta^2 \\
&C = -\xi + 2\xi\eta - \xi\eta^2 \\
&D = \xi\eta - \xi\eta^2 \\
&E = \xi\eta^2 \\
&F = \eta^2 - \xi\eta^2
\end{aligned}
$$

And lastly, for species 'C':

$$\underline{\dot{c}_C} = \begin{bmatrix} \dot{c}_{1,C} \\ \dot{c}_{2,C} \\ \dot{c}_{3,C} \\ \dot{c}_{4,C} \end{bmatrix}$$

Combining the system of Eqs. (2.23.a-c), we obtain the single formulation that describes the problem:

$$\left[\begin{bmatrix} 1 & & & & & & & & & & & \\ & 1 & & & & & & & & & & \\ & & 1 & & & & & & & & & \\ & & & 1 & & & & & & & & \\ & & & & \det J_e/9 & \det J_e/18 & \det J_e/36 & \det J_e/18 & & & & \\ & & & & \det J_e/18 & \det J_e/9 & \det J_e/18 & \det J_e/36 & & & & \\ & & & & \det J_e/36 & \det J_e/18 & \det J_e/9 & \det J_e/18 & & & & \\ & & & & \det J_e/18 & \det J_e/36 & \det J_e/18 & \det J_e/9 & & & & \\ & & & & & & & & 1 & & & \\ & & & & & & & & & 1 & & \\ & & & & & & & & & & 1 & \\ & & & & & & & & & & & 1 \end{bmatrix} \begin{bmatrix} \dot{c}_{1,A} \\ \dot{c}_{2,A} \\ \dot{c}_{3,A} \\ \dot{c}_{4,A} \\ \dot{c}_{1,B} \\ \dot{c}_{2,B} \\ \dot{c}_{3,B} \\ \dot{c}_{4,B} \\ \dot{c}_{1,C} \\ \dot{c}_{2,C} \\ \dot{c}_{3,C} \\ \dot{c}_{4,C} \end{bmatrix} + D \det J_e \begin{bmatrix} & & & & & & & & & & & \\ & & & & & & & & & & & \\ & & & & & & & & & & & \\ & & & & & & & & & & & \\ & & & & G & H & I & J & & & & \\ & & & & K & L & M & N & & & & \\ & & & & O & P & Q & R & & & & \\ & & & & S & T & U & V & & & & \\ & & & & & & & & & & & \\ & & & & & & & & & & & \\ & & & & & & & & & & & \\ & & & & & & & & & & & \end{bmatrix} \begin{bmatrix} c_{1,A} \\ c_{2,A} \\ c_{3,A} \\ c_{4,A} \\ c_{1,B} \\ c_{2,B} \\ c_{3,B} \\ c_{4,B} \\ c_{1,C} \\ c_{2,C} \\ c_{3,C} \\ c_{4,C} \end{bmatrix}\right]$$

$$= FirstPart$$

and the second part of the equation:

$$\sum_{e=1}^{N_\Delta}\left[\begin{array}{l} k\begin{bmatrix} 1 &&&&&&&&&&& \\ & 1 &&&&&&&&&& \\ && 1 &&&&&&&&& \\ &&& 1 &&&&&&&& \\ &&&& {}^{\det Je}\!/\!_{16} & {}^{\det Je}\!/\!_{48} & {}^{\det Je}\!/\!_{144} & {}^{\det Je}\!/\!_{48} &&&& \\ &&&& {}^{\det Je}\!/\!_{48} & {}^{\det Je}\!/\!_{16} & {}^{\det Je}\!/\!_{48} & {}^{\det Je}\!/\!_{144} &&&& \\ &&&& {}^{\det Je}\!/\!_{144} & {}^{\det Je}\!/\!_{48} & {}^{\det Je}\!/\!_{16} & {}^{\det Je}\!/\!_{48} &&&& \\ &&&& {}^{\det Je}\!/\!_{48} & {}^{\det Je}\!/\!_{144} & {}^{\det Je}\!/\!_{48} & {}^{\det Je}\!/\!_{16} &&&& \\ &&&&&&&& -1 &&& \\ &&&&&&&&& -1 && \\ &&&&&&&&&& -1 & \\ &&&&&&&&&&& -1 \end{bmatrix}\begin{bmatrix} c_{1,A}c_{1,B} \\ c_{2,A}c_{2,B} \\ c_{3,A}c_{3,B} \\ c_{4,A}c_{4,A} \\ c_{1,A}c_{1,B} \\ c_{2,A}c_{2,B} \\ c_{3,A}c_{3,B} \\ c_{4,A}c_{4,B} \\ c_{1,A}c_{1,B} \\ c_{2,A}c_{2,B} \\ c_{3,A}c_{3,B} \\ c_{4,A}c_{4,B} \end{bmatrix} \\ + FirstPart \end{array}\right] = 0$$

(2.24)

where the blank spaces within the matrices are equal to zero and:

$$G=\frac{N_r{}^2}{3a^2}+\frac{N_z^2}{3b^2}-\frac{N_r}{a}\iint\limits_{\Omega_0}\frac{A}{r(\xi,\eta)}d\xi d\eta$$

$$H=\frac{-N_r{}^2}{3a^2}+\frac{N_z^2}{6b^2}+\frac{N_r}{a}\iint\limits_{\Omega_0}\frac{A}{r(\xi,\eta)}d\xi d\eta$$

$$I=\frac{-N_r^2}{6a^2}+\frac{-N_z^2}{6b^2}-\frac{N_r}{a}\iint\limits_{\Omega_0}\frac{B}{r(\xi,\eta)}d\xi d\eta$$

$$J=\frac{N_r^2}{6a^2}+\frac{-N_z^2}{3b^2}+\frac{N_r}{a}\iint\limits_{\Omega_0}\frac{B}{r(\xi,\eta)}d\xi d\eta$$

$$K=\frac{-N_r{}^2}{3a^2}+\frac{N_z^2}{6b^2}-\frac{N_r}{a}\iint\limits_{\Omega_0}\frac{C}{r(\xi,\eta)}d\xi d\eta$$

$$L=\frac{N_r{}^2}{3a^2}+\frac{N_z^2}{3b^2}+\frac{N_r}{a}\iint\limits_{\Omega_0}\frac{C}{r(\xi,\eta)}d\xi d\eta$$

$$M=\frac{N_r^2}{6a^2}+\frac{-N_z^2}{3b^2}-\frac{N_r}{a}\iint\limits_{\Omega_0}\frac{D}{r(\xi,\eta)}d\xi d\eta$$

$$N=\frac{-N_r^2}{6a^2}+\frac{-N_z^2}{6b^2}+\frac{N_r}{a}\iint\limits_{\Omega_0}\frac{D}{r(\xi,\eta)}d\xi d\eta$$

$$O=\frac{-N_r^2}{6a^2}+\frac{-N_z^2}{6b^2}+\frac{N_r}{a}\iint\limits_{\Omega_0}\frac{D}{r(\xi,\eta)}d\xi d\eta$$

$$P=\frac{N_r^2}{6a^2}+\frac{-N_z^2}{3b^2}-\frac{N_r}{a}\iint\limits_{\Omega_0}\frac{D}{r(\xi,\eta)}d\xi d\eta$$

$$Q=\frac{N_r{}^2}{3a^2}+\frac{N_z^2}{3b^2}-\frac{N_r}{a}\iint\limits_{\Omega_0}\frac{E}{r(\xi,\eta)}d\xi d\eta$$

$$R=\frac{-N_r{}^2}{3a^2}+\frac{N_z^2}{6b^2}+\frac{N_r}{a}\iint\limits_{\Omega_0}\frac{E}{r(\xi,\eta)}d\xi d\eta$$

$$S=\frac{N_r^2}{6a^2}+\frac{-N_z^2}{3b^2}+\frac{N_r}{a}\iint\limits_{\Omega_0}\frac{B}{r(\xi,\eta)}d\xi d\eta$$

$$T=\frac{-N_r^2}{6a^2}+\frac{-N_z^2}{6b^2}-\frac{N_r}{a}\iint\limits_{\Omega_0}\frac{B}{r(\xi,\eta)}d\xi d\eta$$

$$U=\frac{-N_r{}^2}{3a^2}+\frac{N_z^2}{6b^2}-\frac{N_r}{a}\iint\limits_{\Omega_0}\frac{F}{r(\xi,\eta)}d\xi d\eta$$

$$V=\frac{N_r{}^2}{3a^2}+\frac{N_z^2}{3b^2}+\frac{N_r}{a}\iint\limits_{\Omega_0}\frac{F}{r(\xi,\eta)}d\xi d\eta$$

2.8 Numerical Integration.

Prior to assembly, the unintegrated portion in Eq. (2.25) must be integrated. Since the *r* term is dependent on whichever element the integration is performed over and given that there is no closed analytical form for the integrand containing the *r* term, numerical integration will be performed. A two point Gaussian quadrature rule will be utilized, which is exact for polynomials to the order three; therefore, there is no error in performing the numerical integration. The following equation is used in integration:

$$
\begin{aligned}
&\int_0^1\int_0^1 f(x,y)\,dx\,dy = \frac{1}{4}\int_{-1}^{1}\int_{-1}^{1} f\left(\left(\frac{1}{2}\xi+\frac{1}{2}\right),\left(\frac{1}{2}\eta+\frac{1}{2}\right)\right)d\xi\, d\eta = \\
&\frac{1}{4}\left[\begin{aligned}
&w_1 w_1 f\left(\left(\frac{1}{2}\xi_1+\frac{1}{2}\right),\left(\frac{1}{2}\eta_1+\frac{1}{2}\right)\right)+w_1 w_2 f\left(\left(\frac{1}{2}\xi_1+\frac{1}{2}\right),\left(\frac{1}{2}\eta_2+\frac{1}{2}\right)\right)+ \\
&w_2 w_1 f\left(\left(\frac{1}{2}\xi_2+\frac{1}{2}\right),\left(\frac{1}{2}\eta_1+\frac{1}{2}\right)\right)+w_2 w_2 f\left(\left(\frac{1}{2}\xi_2+\frac{1}{2}\right),\left(\frac{1}{2}\eta_2+\frac{1}{2}\right)\right)
\end{aligned}\right]
\end{aligned}
\qquad (2.25)
$$

where the Christoffel weights w_1 - w_2 are equal to 1 and ξ_1, ξ_2, η_1 and η_2 are roots of Legendre polynomials of degree 2 and are equal to (1/sqrt(3)), -(1/sqrt(3)), (1/sqrt(3)) and -(1/sqrt(3)), respectively.

2.9 Eliminating the Time Derivative.

Our system, Eq. (2.24), now is a nonlinear system of ordinary differential equations with respect to time:

$$\sum_{e=1}^{N_\Delta}\left[\begin{matrix}\begin{bmatrix}\dot{c}_{1,A}\\ \dot{c}_{2,A}\\ \dot{c}_{3,A}\\ \dot{c}_{4,A}\\ \dot{c}_{1,B}\\ \dot{c}_{2,B}\\ \dot{c}_{3,B}\\ \dot{c}_{4,B}\\ \dot{c}_{1,C}\\ \dot{c}_{2,C}\\ \dot{c}_{3,C}\\ \dot{c}_{4,C}\end{bmatrix}\begin{bmatrix}AA & . & . & (1,12)\\ . & & & \\ . & & & \\ . & & & \\ . & & & \\ . & & & \\ . & & & \\ . & & & \\ . & & & \\ . & & & \\ . & & & \\ (12,1) & & & (12,12)\end{bmatrix}+\begin{bmatrix}c_{1,A}\\ c_{2,A}\\ c_{3,A}\\ c_{4,A}\\ c_{1,B}\\ c_{2,B}\\ c_{3,B}\\ c_{4,B}\\ c_{1,C}\\ c_{2,C}\\ c_{3,C}\\ c_{4,C}\end{bmatrix}\begin{bmatrix}AB & . & . & (1,12)\\ . & & & \\ . & & & \\ . & & & \\ . & & & \\ . & & & \\ . & & & \\ . & & & \\ . & & & \\ . & & & \\ . & & & \\ (12,1) & & & (12,12)\end{bmatrix}+\\ \begin{bmatrix}c_{1,A}c_{1,B}\\ c_{2,A}c_{2,B}\\ c_{3,A}c_{3,B}\\ c_{4,A}c_{4,A}\\ c_{1,A}c_{1,B}\\ c_{2,A}c_{2,B}\\ c_{3,A}c_{3,B}\\ c_{4,A}c_{4,B}\\ c_{1,A}c_{1,B}\\ c_{2,A}c_{2,B}\\ c_{3,A}c_{3,B}\\ c_{4,A}c_{4,B}\end{bmatrix}\begin{bmatrix}AC & . & . & (1,12)\\ . & & & \\ . & & & \\ . & & & \\ . & & & \\ . & & & \\ . & & & \\ . & & & \\ . & & & \\ . & & & \\ . & & & \\ (12,1) & & & (12,12)\end{bmatrix}\end{matrix}\right]=0$$

or (2.26)

$$\sum_{e=1}^{N_\Delta}\left[\underline{\underline{AA}}\bullet\underline{\dot{c}_{A-C}(t_n)}+\underline{\underline{AB}}\bullet\underline{c_{A-C}(t_n)}+\underline{\underline{AC}}\bullet\underline{c_A c_B(t_n)}\right]=0$$

where the matrices **AA** - **AC** are the corresponding local matrices in Eq. (2.24).

The *Crank-Nicholson Method* will now be invoked in order to approximate $c(t_n)$ and its time derivative:

$$\begin{aligned}\dot{c}(t_n)&=\frac{\left(c^n-c^{n-1}\right)}{\Delta t}\\ c(t_n)&=\frac{\left(c^n+c^{n-1}\right)}{2}\end{aligned}\qquad(2.27)$$

where c^n and c^{n-1} correspond to the values of these constants at time (t) = n and $t = n - 1$, respectively and Δt is the time step used. In this manner, the time derivatives are approximated by the values of the constants at $t = n -1$ and $t = n$, after which the values of c^n can be obtained:

$$\sum_{e=1}^{N_\Delta}\left(\begin{array}{l}\frac{\underline{\underline{\underline{AA}}}}{\Delta t}\bullet\underline{c^{n}_{A-C}}+\frac{-\underline{\underline{\underline{AA}}}}{\Delta t}\bullet\underline{c^{n-1}_{A-C}}+\frac{\underline{\underline{\underline{AB}}}}{2}\bullet\underline{c^{n}_{A-C}}+\frac{\underline{\underline{\underline{AB}}}}{2}\bullet\underline{c^{n-1}_{A-C}}+\\ \frac{\underline{\underline{\underline{AC}}}}{4}\bullet\underline{c^{n}_{A}c^{n}_{B}}+\frac{\underline{\underline{\underline{AC}}}}{4}\bullet\underline{c^{n-1}_{A}c^{n}_{B}}+\frac{\underline{\underline{\underline{AC}}}}{4}\bullet\underline{c^{n}_{A}c^{n-1}_{B}}+\frac{\underline{\underline{\underline{AC}}}}{4}\bullet\underline{c^{n-1}_{A}c^{n-1}_{B}}\end{array}\right)=0 \tag{2.28}$$

In this case, for each time step, we obtain a nonlinear system containing the unknown constants c^n.

The Crank-Nicholson Method was chosen due to its accuracy and stability (i.e., error stays bounded regardless of time-step size).

2.10 Solving the Nonlinear System.

After assembling the local matrices and forming the global matrices (Figure 2.2), we can express Eq. (2.28) as a vector $F(c^n)$:

$$\underline{F(c^n)}=\begin{bmatrix} f_1(c^n) \\ . \\ . \\ f_{3(N_\Delta+N_r+N_z+1)}(c^n)\end{bmatrix} \tag{2.29}$$

which contains the functions f_1 through $f_{3(N_\Delta+N_r+N_z+1)}$ ($N_\Delta + N_r + N_z + 1$ is the total number of vertices within the mesh and the multiplication factor of 3 is used to account for the existence of 3 species in this system).

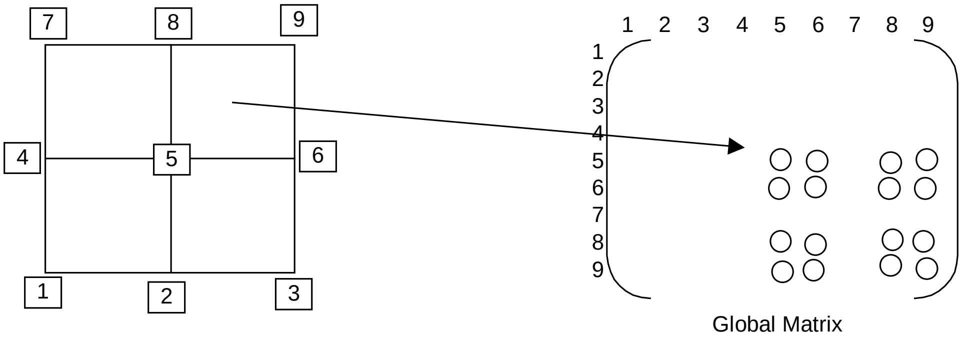

Figure 2.2 Assembling the Global Matrices.

The Jacobian of Eq. (2.29) is a matrix of dimension *3(NΔ+Nr+Nz+1) X 3(NΔ+Nr+Nz+1) and* contains the partial derivatives of the functions with respect to each of the unknown constants:

$$\underline{\underline{J(c^n)}} = \begin{bmatrix} \dfrac{\partial f_1(c^n)}{\partial c_1^n} & \cdot \quad \cdot & \dfrac{\partial f_1(c^n)}{\partial c_{3(N_\Delta + N_r + N_z + 1)}^n} \\ \cdot & \cdot & \cdot \\ \cdot & \cdot & \cdot \\ \dfrac{\partial f_{3(N_\Delta + N_r + N_z + 1)}(c^n)}{\partial c_1^n} & \cdot \quad \cdot & \dfrac{\partial f_{3(N_\Delta + N_r + N_z + 1)}(c^n)}{\partial c_{3(N_\Delta + N_r + N_z + 1)}^n} \end{bmatrix} \tag{2.30}$$

We can now invoke the Newton method to interatively solve this algebraic problem. It consists of solving the following system, using an initial guess for the vector $c^{n,1}$:

$$\begin{gathered} \underline{F\left(c^{n,1}\right)} + \underline{\underline{J\left(c^{n,1}\right)}} \bullet \underline{\left(c^{n,2} - c^{n,1}\right)} = 0 \\ or \\ \underline{-F\left(c^{n,1}\right)} = \underline{\underline{J\left(c^{n,1}\right)}} \bullet \underline{\left(c^{n,2} - c^{n,1}\right)} \end{gathered} \tag{2.31}$$

Now, by initially guessing the vector $c^{n,1}$, we can calculate *F* and *J*. This results in a linear algebraic system which we can solve for the vector $c^{n,2}$ - $c^{n,1}$ (done using LINPACK routines). After addition of $c^{n,1}$, the vector $c^{n,2}$ is obtained, which serves as the next guess in the iteration loop. After a desired tolerance is reached, the solution for that time step is obtained.

2.11 Model Verification and Sample Model.

Before the model is applied to experimental work, its accuracy must first be verified. In this case, diffusion and reaction will be verified separately: reaction will be verified by an analytical solution and diffusion within the finite cylinder will be verified using a series solution.

The infinite series representation of the solution to binary Fickian diffusion within a finite cylinder is given by the following equation:

$$\begin{gathered} \frac{M_\infty - M_t}{M_\infty} = \frac{32}{\pi^2} \cdot \sum_{m=1}^{\infty} \frac{1}{(\alpha_m R)^2} \exp\left[-\frac{(\alpha_m R)^2}{R^2} Dt \right] \cdot \\ \sum_{n=0}^{\infty} \frac{1}{(2n+1)^2} \exp\left[-\frac{(2n+1)^2 \pi^2}{4L^2} Dt \right] \end{gathered} \tag{2.32}$$

in which:

M_∞ = final mass of diffusing substance
M_t = mass of diffusing substance at time = t
R = radius of the cylinder
L = half height of the cylinder
α_m = roots of $J_0(\alpha_m R) = 0$

The diffusion aspect of this model was simulated using a 5X10 dimensionless length units and a 5X10 mesh. The diffusion coefficient used was 2 (dimensionless) with a reaction rate constant of 0. The time step size used was 1/5 dimensionless reciprocal time. The initial boundary condition for diffusing substance was 10 dimensionless concentration units. The simulated concentration profile was numerically integrated to give total amount of diffusing substance. The total amount of diffusing substance is plotted as a function of time for both the finite element model and the series solution (Figure 2.3). As can be seen, there is good agreement between the finite element solution and the series solution.

The reaction term can be solved analytically by integrating Eq. (2.1.a) to yield:

$$\begin{aligned} \int_{[a_1]}^{[a_2]} \frac{\partial[a]}{a} &= -k[b]\int_{t_1}^{t_2} \partial t \\ \ln\frac{[a_2]}{[a_1]} &= -k[b](t_2 - t_1) \end{aligned} \tag{2.33}$$

By setting the diffusion coefficient to 0, the reaction can be observed in the boundary element vertices. The reaction rate constant used was 0.02 (dimensionless), with initial conditions of 30 for the immobile reacting species and 10 for the mobile reactant (all dimensionless concentration units. The time step size used is 0.2. The immobile reacting species concentration vs. time is plotted for the analytical solution and the numerical solution (Figure 2.4). Again, there is excellent agreement.

The model output reflects the concentration distributions of all of the chemical species over space. A sample calculation is shown for a 5X10 cylinder quarter with a 5X10 mesh. The diffusion coefficient is 2 and the reaction rate constant is 0.02. The initial concentration of immobile reactant is 30 while the boundary condition for the diffusing reactant is 10. The total time of diffusion and reaction is 4 with a time step size of 0.2. The concentration distribution of remaining immobile reactant groups is shown in Figure 2.5.

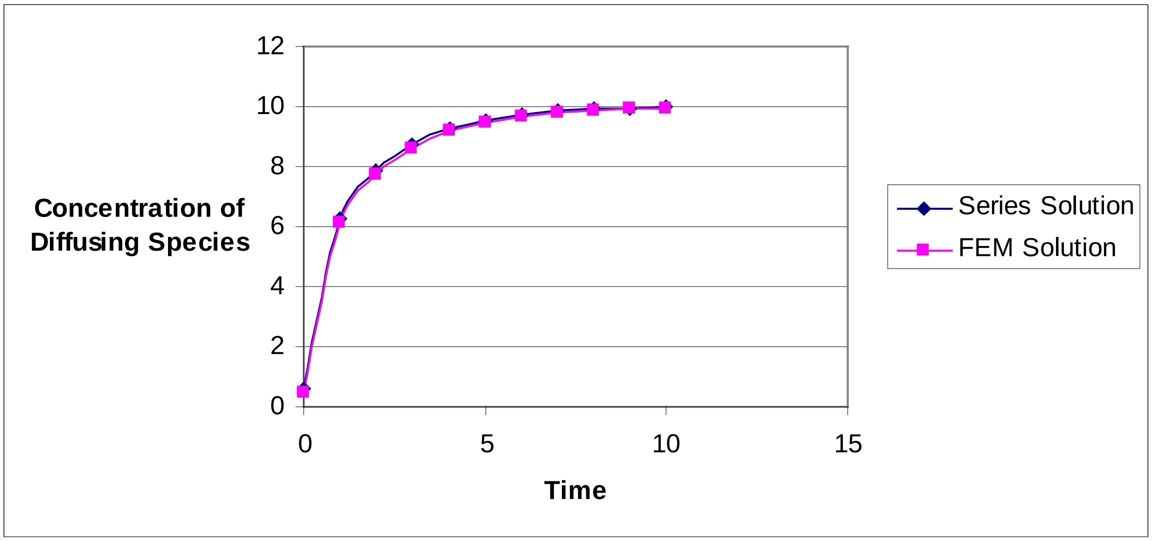

Figure 2.3 Comparison of Total Amounts of Diffusing Substance vs. Time for the Series Solution and FEM Solution.

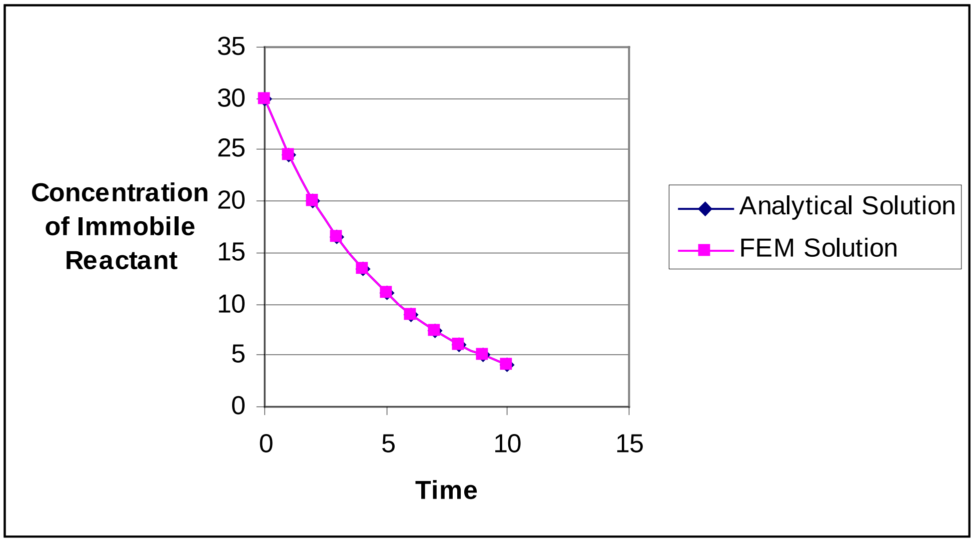

Figure 2.4 Comparison of Immobile Reactant Concentrations vs. Time for the Analytical Solution and FEM Solution.

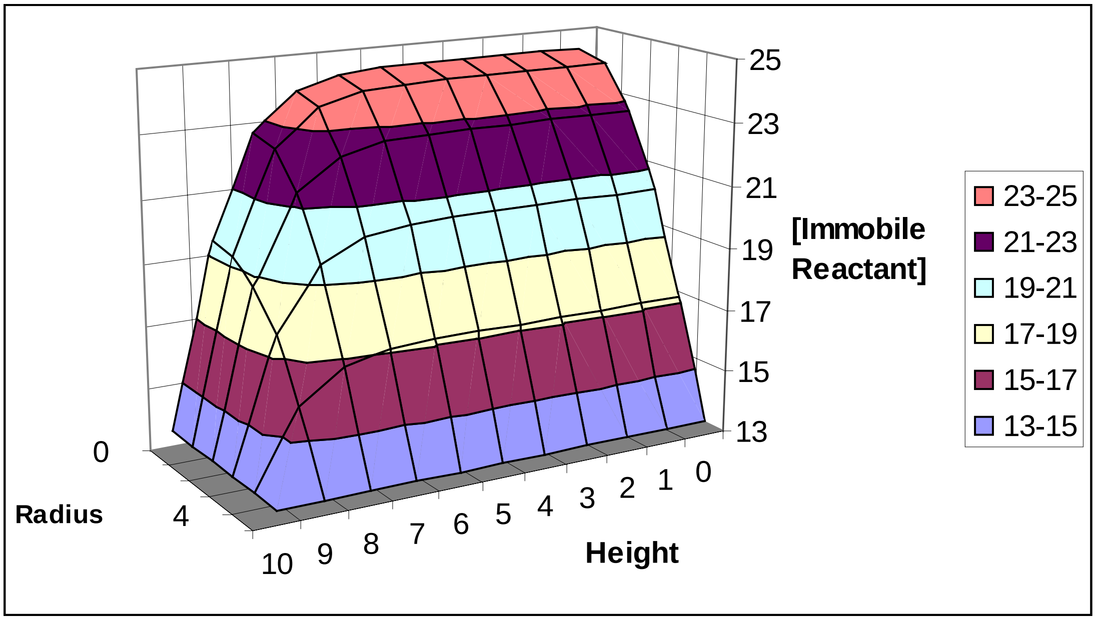

Figure 2.5 Solution: Immobile Group Concentration Distribution.

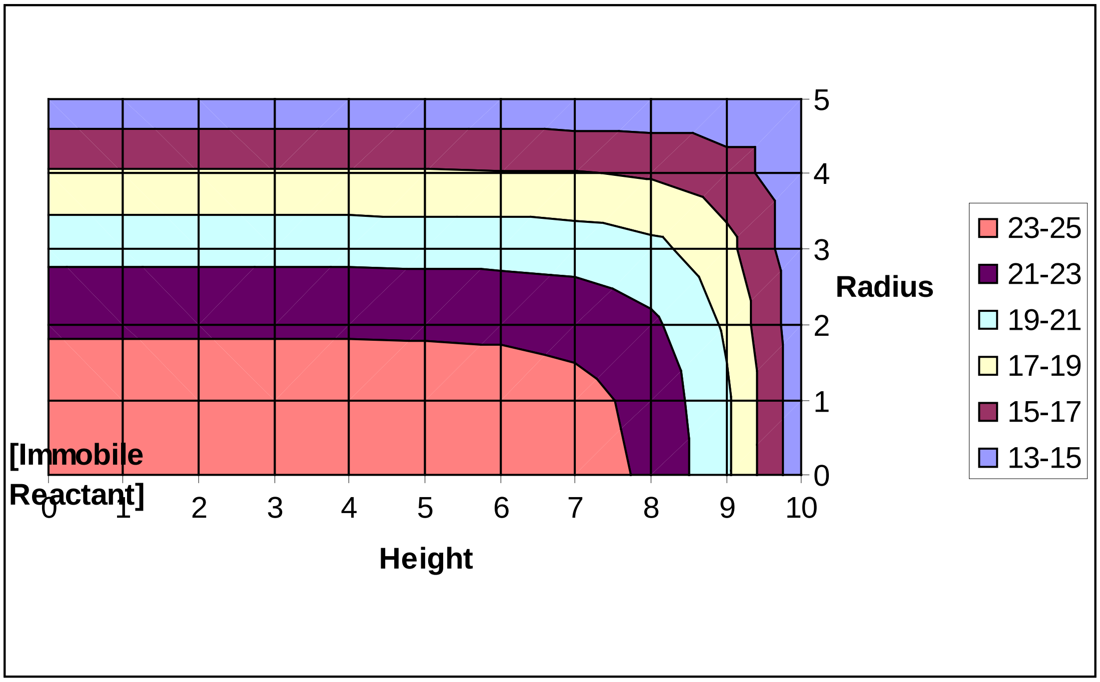

2.12 Conclusions.

A finite element model was employed to describe the reaction / diffusion system found in chemical modification of polymeric fibers to be used as reinforcement. The model generated was extremely rudimentary, using bi-linear shape functions with rectangular elements. However, the model was found to accurately predict diffusion and reaction solutions when compared with the series and analytical solutions, respectively.

Further directions regarding this model include:

1. Fitting of the model solution with the experimental system,
2. Incorporation of a nonconstant diffusion coefficient which depends on diffusing species concentration and fiber morphology,
3. Incorporation of a different diffusion coefficient for the product species and
4. A variable density depending on whether the solid is crystalline cellulose, noncrystalline cellulose, or cellulose acetate.

Experimental measurement of the acetyl group concentration as a function of time during reaction can be carried out by the use of surface analysis techniques. One such technique is attenuated total reflectance infrared spectroscopy (ATR-IR). This technique is easiest to carry out using nearly flat surfaces, in which case a suitable replacement for the cellulose fiber would have to be found. A morphologically similar cellulose film produced from solution (NMMO) would be ideal. Once such a sheet has been obtained, acetylation combined with quantitative surface analysis can be used to obtain pure reaction parameters (order and rate constant).

However, obtaining the diffusion parameters (i.e., diffusion coefficient) may prove to be quite difficult. The experimental data needed in this case are either an overall average concentration of remaining hydroxyl groups over the course of the diffusing reaction or the actual concentration profile as a function of time. An average concentration of acetyl groups may be obtained by a modified aminolysis/GC procedure (see *Methods* section of Chapters 3 and 4) which is capable of measuring extremely low acetyl contents. Titration may also offer a solution to this problem of collection the necessary data.

A first approximation to diffusion in this system could then be obtained by simply varying the diffusion coefficient to best fit the data (it is the only variable left after obtaining the reaction parameters). However, this is empirical at best and does not accurately reflect the real differences in diffusion through parts of the fiber with varying morphology, parts of the fiber with differing degrees of substitution and the expected concentration dependence of the diffusion coefficient itself. Isolating these different effects and then quantifying them would prove very difficult indeed.

CHAPTER 3.

Experimental: Biobased Composites from Modified Fibers-Cellulose Acetate Butyrate with Acetylated Lyocell.

3.0 Abstract.

In the initial study of the cellulose fiber/thermoplastic CAB composite system, composites were fabricated using a variety of methods using woven fabric reinforcement. Tensile tests were then performed, followed by microscopic evaluation of the fracture surfaces. These visualizations revealed a large amount of fiber pullout [Glasser and Davis, 1999] during composite failure. Poor interfacial adhesion was viewed as a possible cause for the fiber pullout.

Fiber surface acetylation then was employed as a potential remedy of this problem. Composites containing unmodified fiber as well as modified fiber were produced and their tensile properties along the fiber direction were measured. Afterwards, composite cross sections as well as fracture surfaces were examined using scanning electron microscopy.

Tensile property evaluation suggested that no significant improvement was gained through the use of a surface acetylated fiber. Maximum strength values were typically in the range of 210 MPa while moduli values were ca. 14 GPa for composites containing close to 10 volume % voids and 40 volume % fiber (including voids). Furthermore, microscopic evaluation revealed very little fiber pull out during composite fracture in both of the composites produced, suggesting relatively adequate fiber/matrix adhesion in both cases. In addition, cross sections revealed good fiber/matrix dispersion within the composite. These new findings as well as the previous study results were interpreted in the following way: the composites in the previous study suffered from lack of tow penetration by the matrix polymer. Once this problem was remedied (in this case by using unidirectional fiber tow instead of woven fabric) and the fiber and matrix were sufficiently contacted, adhesion between these two phases was found to follow suit.

3.1 Introduction.

Previous work on the CAB/cellulose fiber composite system indicated a possible deficiency regarding fiber/matrix adhesion [Glasser and Davis, 1999]. This was evidenced by the large amount of fiber pullout observed during composite fracture. Furthermore, a previous study utilizing cellulosic fibers within a CAB matrix [Glasser *et al.*, 1999] revealed a general lack of adhesion between these two materials. Therefore the objectives of this study are twofold: (1) to clarify and characterize the interface between cellulose and CAB and (2) to determine whether fiber surface acetylation improves the interfacial behavior between cellulose and CAB.

3.2 Experimental.

3.2.0 Materials.

Matrix: Cellulose acetate butyrate (CAB 381-20), henceforth denoted as CAB, was obtained in powder form from Eastman Chemical Company, Kingsport, Tennessee. The average acetyl and butyryl contents were 13.5 and 38.1 wt.% and the falling ball viscosity was 20 seconds (76 poise). The number average molecular weight (M_N) was 69,600 with molecular weight distribution of 1.83 (Figure 3.0.a).

Fibers: The continuous cellulose fibers used in this study are termed 'Lyocell,' and are produced by regeneration from N-methylmorpholine-oxide (Figure 3.0.b). Lyocell fibers were supplied by Acordis of England. The tows consisted of 16,700 filaments, each ca. 11 micrometers in diameter and 1.1 dTex[1]. The fibers were spun using a line speed of 60 m/min. The fibers used for this study did not have any coating or finish. The modulus of Lyocell fibers has been reported in the range of 12 to 20 GPa depending on fiber draw ratio during manufacturing [Mortimer *et al.*, 1996]. Bourban *et al*. [1997] reported the use of Lyocell fibers of undisclosed origin with a modulus of 36 GPa. The reported elongation at break values range from 11 to 17%.

Acetylated Fibers: 16 meters of Lyocell tow were suspended above 200 ml of acetic anhydride in a Parr (Moline, IL) pressure reactor. The reactor was then evacuated using an aspirator. The reactor temperature was then raised to 150 °C where it was held constant for 24 hours. Afterwards, the fibers were quenched in a water bath for 8 hours, then dried overnight in a laboratory hood and subsequently overnight in a vacuum oven at room temperature. This resulted in acetylated Lyocell fibers (Figure 3.0.c) under heterogeneous conditions. Confirmation of fiber acetylation was qualitatively carried out using FTIR spectroscopy using the absorption peak centered around 1748 cm^{-1}.

---

[1] Tex = grams per 1000 meters of fiber

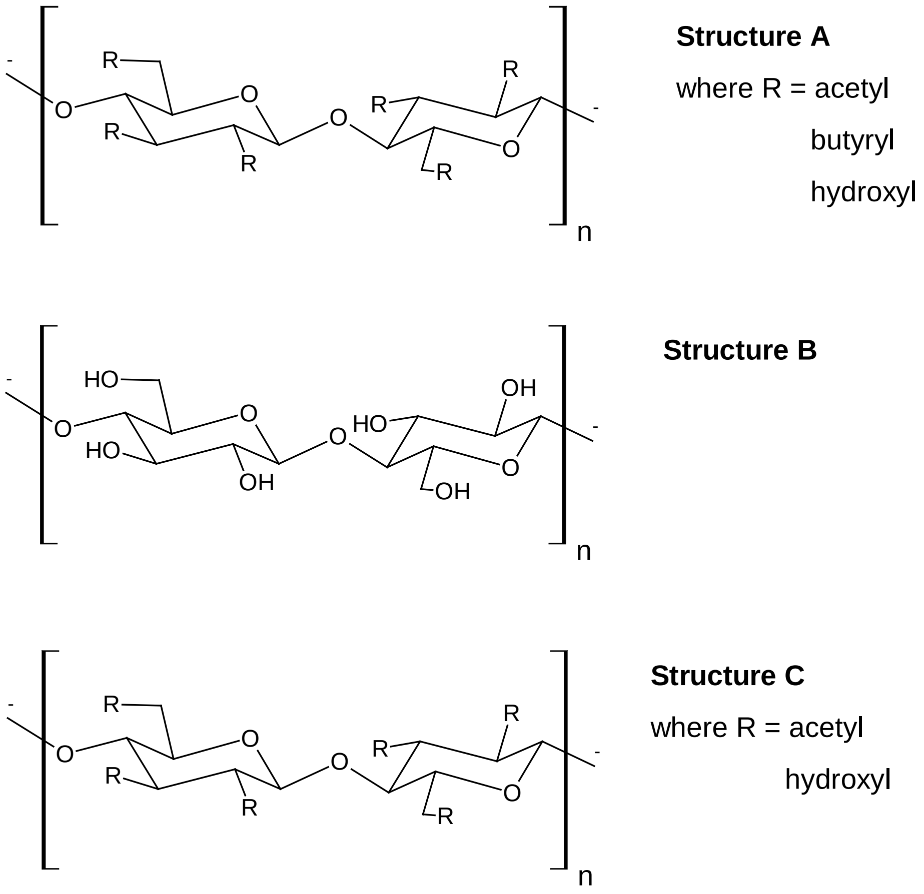

Figure 3.0 Chemical Constituents: (A.) CAB; (B.) cellulose; and (C.) cellulose acetate.

3.2.1 Methods.

Preparation of Unidirectional Composite Prepregs: The fiber tows were preimpregnated ('prepregged') using a 12 % (w/w) solution of CAB in acetone. Acetone was chosen as the prepregging solvent because of high volatility and ease of handling. Both acetylated fibers and unacetylated fibers were used. The fiber tow was passed through the solution at a constant rate and then wound around a 6-inch square aluminum plate (Figure 3.1). Fiber tow was laid down side by side without overlap, covering both sides of the plate with continuous tow. Four layers of tow were successively laid down without allowing the previous layer to dry. Afterwards, the prepreg was allowed to dry overnight in a laboratory hood.

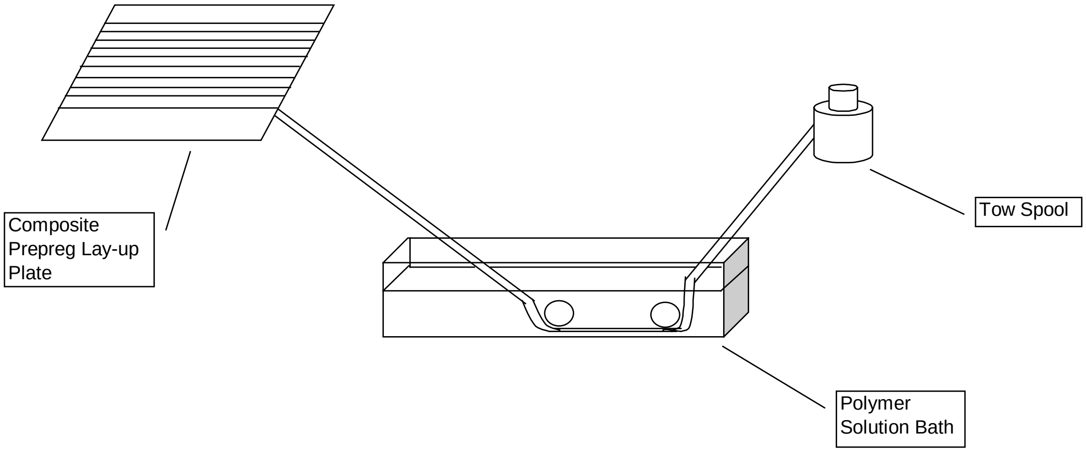

Figure 3.1 Solution Prepregging Process.

Melt Consolidation of Unidirectional Composite Prepregs: Prepregs (still wrapped around metal plate) were sandwiched between release film and two 6-inch square aluminum plates. These were then consolidated under heat and pressure in a Carver laboratory press. The prepregs were preheated at a temperature of 200 °C without pressure for two minutes.

The pressure was then raised to a pressure of ca. 1 metric ton, using one-millimeter spacers on each side of the prepregged tow. The temperature was held constant.

Fiber Content Analysis: Fiber volume fraction determination was conducted using gas chromatography. This procedure was originated by Mansson and refined by Samaranayake and Glasser [1993]. The procedure used ca. 27 mg neat CAB sample and ca. 60 mg. composite sample. The samples were suspended in 2 mL of internal standard solution. This solution comprised of 90.4 mg hexanoyl pyrrolidine in 9 ml of a 1:1 (by volume) mixture of pyrrolidine and pyridine. The reaction mixtures were then reacted in a glass vial with a triangular magnetic stir bar and a Reactivial (Supelco) fitting. The reaction took place for 23.5 hours at a temperature of 80 °C. After cooling, the sample mixture was filtered and 5 microliters was injected into the gas chromatograph (GC). A Hewlett Packard model 6890 GC equipped with a capillary column was used along with helium as the carrier gas to separate the reaction mixture. The GC conditions used are outlined in Table 3.0.

After the amount of butyryl pyrrolidine derivative in each sample was determined using GC, the fiber volume fractions were determined by back-calculation[2].

Density Analysis: After conditioning in the laboratory environment for greater than 40 hours, the densities of fiber tow, neat CAB and final composites were determined

---

[2] Refer to Appendix B for a sample calculation.

3.0 GC Conditions used in Fiber Content Analysis.

Retention Time of Acetyl Pyrrolidine (min.)	3.1
Retention Time of Butyryl Pyrrolidine (min.)	5.6
Retention Time of Hexanoyl Pyrrolidine (min.)	13.6
Initial Column Temperature (°C; min.)	120; 10
Column Temperature Gradient (°C/min.)	4
Final Column Temperature (°C/min.)	140; 2
Injector Temperature (°C)	200
Split Flow Ratio	75.025:1
Detector Temperature (°C)	275
He Flow Rate (cc/min.)	2.6

using ASTM D792, Test Method B with isopropyl alcohol[3] as the test liquid. This Table procedure utilizes displacement in order to determine apparent density (D^{23C}). The calculation was carried out in the following manner:

$$D^{23C}(kg/m^3) = 780\frac{a}{(a-b)} \tag{3.0}$$

where: a = apparent mass of specimen in air
b = apparent mass of specimen completely immersed in liquid

Upon determination of fiber volume contents and composite densities, void volumes of each composite prepared were then determined. The theoretical density of a fully consolidated composite (ρ_t) can be calculated using the following equation:

$$\rho_t = \frac{\rho_f \rho_m}{W_f \rho_m + W_m \rho_f} \tag{3.1}$$

in which the subscripts *m* and *f* represent matrix and fiber, respectively, and *W* represents weight fraction. The void volume (X_v) follows:

$$X_v = \frac{\rho_t - \rho_e}{\rho_t} \tag{3.2}$$

Density measurements were made on ca. one inch square specimens.

Tensile Testing of Composites Along the Fiber Direction: Rectangular specimens were cut from composite panels using a fine bandsaw and measured 10 cm (4 inches) long, 1.25 cm (0.5 inches) wide and ca. 1.2 mm in thickness. Tensile tests were performed using an Instron Testing Machines model 4204 with a load beam of 5 kN in a laboratory environment. The crosshead speed was kept at 2 mm/min for all tests. Strain

---

[3] Water cannot be used in this case because of extensive absorption into cellulose. See Appendix E.

was measured using an MTS strain gauge. The tests were conducted at room temperature. Reported data points represent the average of at least 3 measurements. Test specimens were conditioned at room conditions for greater than 40 hours. Modulus figures were measured by taking the slope between 0.1 and 0.5 % strain (ca. 25 % of failure strain). Statistics used include the mean (*x bar*), standard deviation (s_{n-1}) and the coefficient of variation (*CV*):

$$\bar{x} = \left(\sum_{i=1}^{n} x_i\right) \Big/ n \tag{3.3}$$

$$s_{n-1} = \sqrt{\left(\sum_{i=1}^{n} x_i^2 - n\bar{x}^2\right) \Big/ (n-1)} \tag{3.4}$$

$$CV = 100 s_{n-1} \big/ \bar{x} \tag{3.5}$$

Scanning Electron Microscopy (SEM): SEM of the composite specimens were performed using an AMRAY 180 D (Diffusion system) Scanning Electron Microscope, at an operating voltage of 10 kV. Razor cut composite cross sections as well as fracture surfaces of the composites were mounted on an aluminum surface and sputter coated with gold in a Denton vacuum DV 515 evaporator.

3.3 Results and Discussion.

3.3.0 Composite Characterization.

Composites containing unacetylated and acetylated fiber tow along with CAB were prepared according to the procedures outlined in the methods section. The original fiber was white but thereafter emerged from the acetylation vessel with a golden color. Likewise, under the application of heat within the hot press, the fibers continued to darken and became brown. This may be attributed to thermal degradation. Since the acetylated fiber composite underwent the application of heat during pressing and acetylation, the resulting panel was darker brown than the unmodified lyocell composite. The issue of whether or not thermal degradation of the reinforcing fibers affects their mechanical properties will be investigated in the next chapter.

The panels produced had the characteristics outlined in Table 3.1. The void contents ranged from 8 volume % for the acetylated fiber composite to 13 vol.% for the unmodified fiber composite. Fiber contents (volume % on a voidless basis) ranged from 43 to 46 for modified composite and unmodified fiber composite, respectively.

Table 3.1 Composite Panel Compositions.

Composite Type	Vol% Air	Avg. Butyryl Content (mg)	Vol% Fiber	Vol% CAB
Unacetylated Fiber Composite	13	21.8	41	46
Acetylated Fiber Composite	8	21.3	40	52

The panels produced had virtually identical fiber volume fractions with the exception that the unacetylated fiber composite contained slightly higher fiber fraction. However, the acetylated fiber content contained a lower percentage of void volume fraction. Fiber volume fraction determination using GC was verified by the determination that the CAB had a 36 wt% butyryl ester content, which agrees well with the stated manufacturer's value of 38 wt% butyryl ester.

3.3.1 Composite Tensile Properties.

Composite specimens were tested in stress strain mode along the fiber direction for both unacetylated fiber composites and acetylated fiber composites. A typical load strain curve for the composites produced is detailed in Figure 3.2.

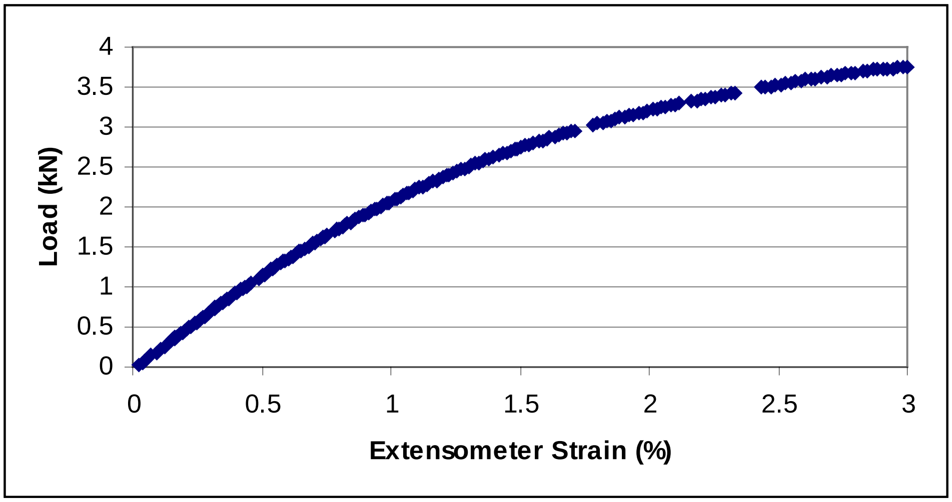

Figure 3.2 Typical Load Strain Curve for Composites Produced.

The maximum strength, strain and moduli data are reported in Table 3.2.

Table 3.2 Tensile Properties of Composite Panels[4].

Sample	**Void Volume (%)**	**Fiber Volume (%, void basis)**		**Max. Strain (%)**	**Std. Deviation**	**COV**
Unacetylated Fiber Composite	13	41		2.49	0.34	13.6
Acetylated Fiber Composite	8	40		2.34	0.58	24.6
	Modulus (GPa)	**Std. Deviation**	**COV**	**Max. Strength (MPa)**	**Std. Deviation**	**COV**
Unacetylated Fiber Composite	13.3	1.08	8.1	199	21.6	10.9
Acetylated Fiber Composite	15.2	2.24	14.8	224	28.1	12.6

As can be seen, the tensile properties and stiffness of the acetylated fiber composites was higher in all cases; however, these properties did not vary beyond one standard deviation. Therefore, acetylation of Lyocell tow does not appear to significantly improve composite tensile properties along the fiber direction.

---

[4] A t-test with alpha = 0.05 reveals that none of the tensile properties are statistically different for the acetylated composite and the unacetylated fiber composite.

3.3.2 SEM Visualizations of Composite Cross Sections and Fracture Surfaces.

Composite cross sections as well as fracture surfaces are shown in Figure 3.3.

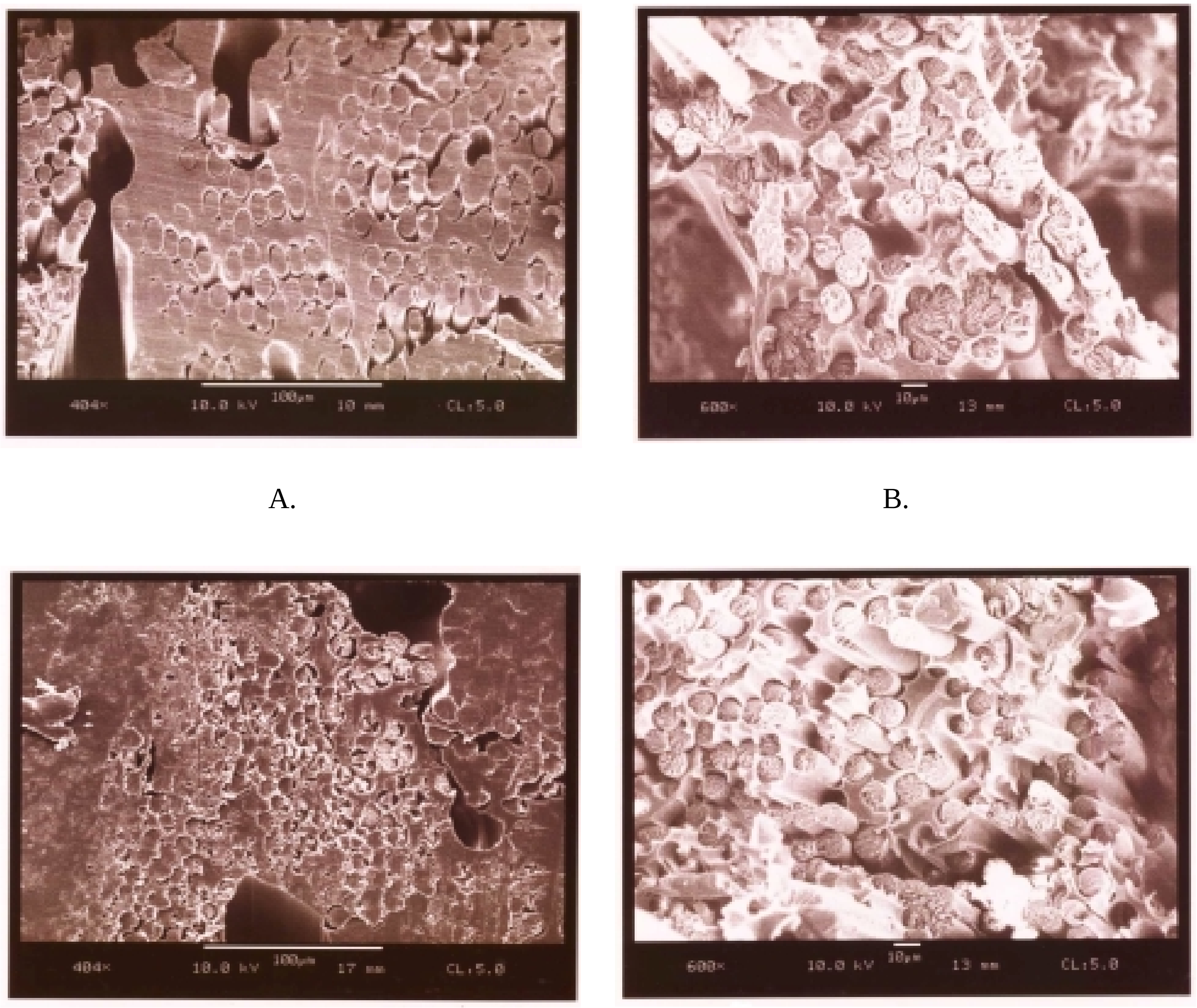

A. B.

C. D.

Figure 3.3 SEM Images of (A.) Unacetylated Lyocell Composite Cross-Section (razor-cut), (B.) Unacetylated Lyocell Composite Fracture Surface, (C.) Acetylated Lyocell Composite Cross-Section (razor-cut) and (D.) Acetylated Lyocell Composite Fracture Surface.

The cross sections of both the unmodified and modified fiber composites reveal relatively good fiber dispersion within the matrix. Few unwetted fibers are observed. Also clearly depicted in the cross section is the presence of voids. These may originate from the layering of prepregged tow without the use of vacuum.

The fracture surfaces of the two composites are virtually identical. The majority of fiber failure surfaces appear flush with the matrix failure surface. There appears to be very little fiber pull out. Since gross fiber-pull out is typically viewed as evidence of poor fiber/matrix adhesion, this system (unmodified as well as acetylated cellulose fiber/CAB) appears to display favorable interaction between the matrix and fiber phases. This is consistent with the tensile results outlined previously.

These results suggest that fiber pull out experienced during the previous study on the CAB/cellulose fiber composite system was a result of inadequate matrix dispersion around the individual filaments rather than lack of fiber/matrix adhesion. This may have resulted from the use of fibers in woven fabric form in the previous study, which can not be effectively spread as unidirectional tow can during solution prepregging.

3.4 Conclusions.

Fiber surface acetylation was employed as a potential remedy of the apparent lack of fiber/matrix adhesion previously observed in the cellulose fiber/CAB composite system [Glasser and Davis, 1999]. Composites containing unmodified fiber as well as modified fiber were produced and their mechanical properties were measured under tension along the fiber direction. Afterwards, composite cross sections as well as fracture surfaces were examined using scanning electron microscopy.

Tensile property evaluation suggested that only a modest improvement was gained through the use of surface acetylated fiber. Maximum strength values were typically in the range of 210 MPa while moduli values were ca. 14 GPa for composites containing close to 10 volume % voids and 40 volume % fiber (including voids). Furthermore, microscopic evaluation revealed very little fiber pull out during composite fracture of both composites produced, suggesting relatively good fiber/matrix adhesion in both cases. Cross sections also reveal good fiber/matrix dispersion within the composite. These findings as well as the previous study results can be interpreted in the following way: the composites in the previous study suffered from lack of tow penetration by the matrix polymer. Once this problem was remedied (in this case by using unidirectional fiber tow instead of woven fabric) and the fiber and matrix were sufficiently contacted, adhesion between these two phases ensued.

CHAPTER 4.

Experimental: Optimizing the Consolidation Process of Cellulose Acetate Butyrate with Lyocell Fiber Prepregs.

4.0 Abstract.

Composites were manufactured at differing consolidation conditions, including temperature, pressure and time using design of experiments methodology. Both interlaminar shear strength (ILSS) and composite void volume were then measured. The results were then analyzed using standard regression techniques. Minimal void contents (ca. 2.83 vol. %) were found to occur at moderate temperatures (200 °C), low consolidation pressures (11.8 p.s.i.) and long times (13 minutes). This was also where interlaminar shear strength was maximized at a value of 16.3 MPa. This agrees relatively well with the mathematical predictions.

Tensile properties did not appear to be significantly affected through the use of excessive consolidation temperatures (230 °C). The highest tensile properties were observed at the ILSS and void volume optimal consolidation condition: a modulus of 22 GPa and a strength of 246 MPa were obtained. Furthermore, microscopic examination of the fracture surfaces indicate that fiber-matrix adhesion is considerable in the absence of any fiber surface modification.

4.1 Introduction.

The previous study considered the adequacy of matrix-fiber adhesion. The objective of this second study was to optimize the composite consolidation process. The three consolidation inputs (pressure, time, temperature) were varied using design of experiments protocol. A regression model was formulated to describe all input linear effects, linear interactions and second order effects, after which composite void content was minimized and apparent interlaminar shear strength was maximized (within the design space). Tensile strength along the fiber direction of the composites was also monitored to ensure that relatively severe temperatures and consolidation times do not negatively affect the fiber/composite integrity.

4.2 Experimental.

4.2.0 Materials.

Matrix: Cellulose acetate butyrate (CAB 381-20), henceforth denoted as CAB, was obtained in powder form from Eastman Chemical Company, Kingsport, Tennessee. The average acetyl and butyryl contents were 13.5 and 38.1 wt.% and the falling ball viscosity was 20 seconds (76 poise). The number average molecular weight (M_N) was 69,600 with molecular weight distribution of 1.83 (Figure 3.0.a).

Fibers: The continuous cellulose fibers used in this study are termed 'Lyocell,' and are produced by regeneration from N-methylmorpholine-oxide (Figure 3.0.b). Lyocell fibers were supplied by Acordis of England. The tows consisted of 16,700 filaments, each ca. 11 micrometers in diameter and 1.4 dTex. The fibers were spun using a line speed of 60 m/min. The fibers used for this study did not have any coating or finish. The modulus of Lyocell fibers have been reported in the range of 12 to 20 GPa depending on fiber draw ratio during manufacturing [Mortimer *et al*., 1996]. Bourban *et al*. [1997] reported the use of Lyocell fibers of undisclosed source with a modulus value of 36 GPa. The reported elongation at break values range from 11 to 17%.

4.2.1 Methods.

Preparation of Unidirectional Composite Prepregs: The fiber tows were preimpregnated ('prepregged') using a 12 % (w/w) solution of CAB in acetone. Acetone was chosen as the prepregging solvent because of high volatility and ease of handling. The continuous fiber tow was prepregged using a fiber sizing apparatus described in Broyles *et al*. [1998]. It essentially consisted of rollers that passed the tow through the polymer solution bath, a drying tower, and then wound around a drum winder (Figure 3.0). The fiber tow was passed through the solution at a constant rate of 1.295 cm/min. The fiber tension was maintained at 5 lbs. using a tensioning bar. Solution prepregged fibers were dried using I.R. radiation heaters as well as forced convection. The surface

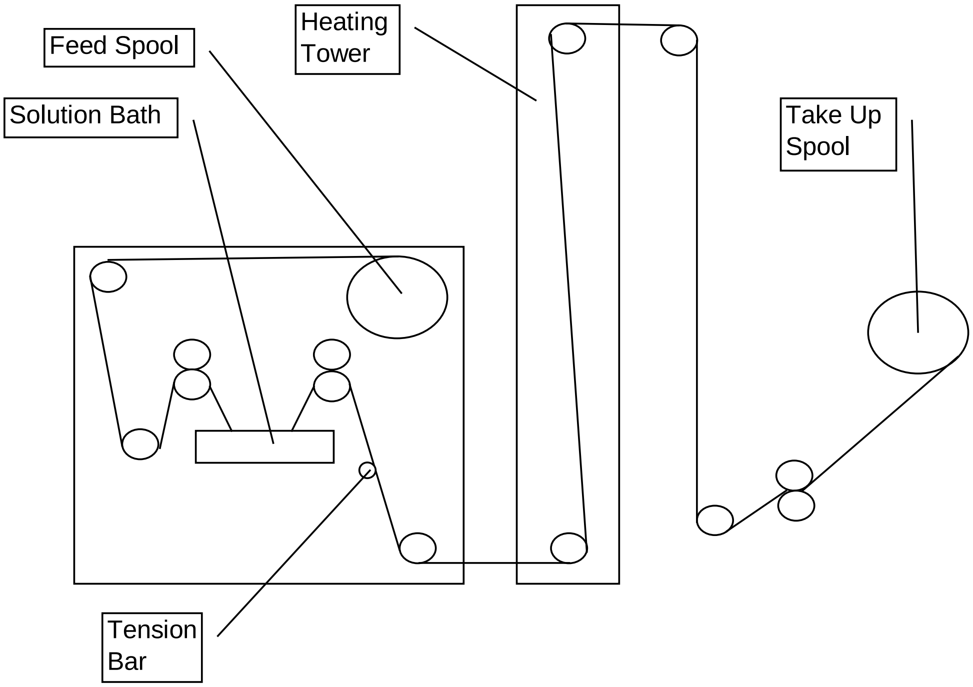

Figure 4.0 Solution Prepregging Process.

temperature of the radiation heaters was kept constant at 130 °C. Fiber tow was laid down side by side on a circular drum with ca. 50 % overlap (tow spacing = 2.66 mm). Once ca. 7 inches of prepregged tow is laid down horizontally on the drum, the tow was cut off the winder in the form of panels. Afterwards, the panels were all vacuum dried at 50 °C for 24 hours to remove residual solvent. These panels were also stitched with nylon upholstery thread prior to consolidation (3 equally spaced rows evenly spaced perpendicular to the fiber direction); stitching was used to combat the effects of fiber dealignment during melt consolidation.

Melt Consolidation of Unidirectional Composite Prepregs: Prepregged panels were stacked unidirectionally three at a time (Figure 4.1). These were then consolidated under varying time, heat and pressure in a Wabash MPI (Wabash, In.) Model V575H-18-BCLPX vacuum press. The press platens were raised to temperatures ranging from 170, 200 and 230 °C. The prepregs were preheated without pressure for two minutes[5].

The pressure was then instantaneously raised to a pressure ranging from 11.8 (500 total lbs.), 23.7 (1000 total lbs.) and 35.5 p.s.i. (1500 total lbs.)[6], for times ranging from 3, 8 and 13 minutes. The temperature was held constant (under vacuum).

---

[5] Refer to Appendix F for a rudimentary discussion of unsteady state heat transfer in the prepregs.

[6] Based on panel dimensions of ca. 6.5 inches X 6.5 inches (42.25 in^2 area).

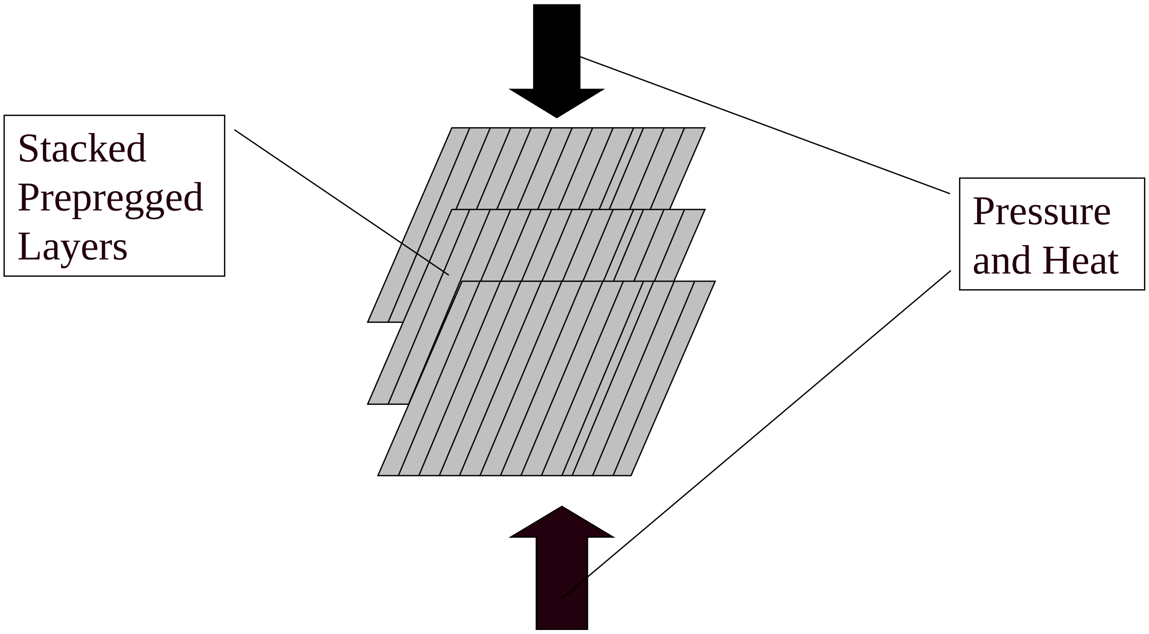

Figure 4.1 Consolidation Process.

Fiber Content Analysis: Fiber volume fraction determination was conducted using gas chromatography. This procedure was originated by Mansson and refined by Samaranayake and Glasser [1993]. The procedure used ca. 27 mg neat CAB sample and ca. 90 mg. composite sample. The samples were suspended in 2 mL of internal standard solution. This solution comprised of ca. 10 mg hexanoyl pyrrolidine per ml of a 1:1 (by volume) mixture of pyrrolidine and pyridine. The reaction mixtures were then reacted in a glass vial with a triangular magnetic stir bar and a Reactivial (Supelco) fitting. The reaction took place for 23.5 hours at a temperature of 80 °C. After cooling, the sample mixture was filtered and 5 microliters was injected into the gas chromatograph (GC). A Hewlett Packard model 6890 GC equipped with a capillary column was used along with helium as the carrier gas to separate the reaction mixture. The GC conditions used are outlined in Table 4.0.

Table 4.0 GC Conditions used in Fiber Content Analysis.

Retention time of Acetyl Pyrrolidine (min.)	3.1
Retention Time of Butyryl Pyrrolidine (min.)	5.6
Retention Time of Hexanoyl Pyrrolidine (min.)	13.6
Initial Column Temperature (°C; min.)	120; 10
Column Temperature Gradient (°C/min.)	4
Final Column Temperature (°C/min.)	140; 2
Injector Temperature (°C)	200
Split Flow Ratio	75.025:1
Detector Temperature (°C)	275
He Flow Rate (cc/min.)	2.6

After the amount of butyryl pyrrolidine derivative in each sample was determined using GC, the fiber volume fractions were determined by back-calculation[7].

Density Analysis: After conditioning in the laboratory environment for greater than 40 hours, the densities of fiber tow, neat CAB and final composites were determined using ASTM D792, Test Method A with isopropyl alcohol as the test liquid. This procedure utilizes displacement in order to determine apparent density (D^{23C}). The calculation was carried out in the following manner:

$$D^{23C}(kg/m^3) = 780\frac{a}{(a-b)} \tag{4.0}$$

where: a = apparent mass of specimen in air
b = apparent mass of specimen completely immersed in liquid

Upon determination of fiber volume contents and composite densities, void volumes of each composite prepared were then determined. The theoretical density (ρ_t) of a fully consolidated composite can be calculated using the following equation:

$$\rho_t = \frac{\rho_f \rho_m}{W_f \rho_m + W_m \rho_f} \tag{4.1}$$

in which the subscripts *m* and *f* represent matrix and fiber, respectively and *W* represents weight fraction. The void volume (X_v) follows:

$$X_v = \frac{\rho_t - \rho_e}{\rho_t} \tag{4.2}$$

Density measurements were taken on ca. two inch square specimens.

Tensile Testing of Composites Along the Fiber Direction: Rectangular specimens were cut from composite panels using a fine bandsaw and measured 10 cm (4 inches) long, 1.25 cm (0.5 inches) wide and ca. 4 mm in thickness. Tensile tests were performed using an Instron Testing Machines model 4204 with a load beam of 15 kN in a laboratory environment. The crosshead speed was kept at 2 mm/min for all tests. Strain was measured using an MTS strain gauge. The tests were conducted at room temperature. Reported data points represent the average of 5 measurements. Test specimens were conditioned at room conditions for greater than 40 hours. Modulus figures were measured by taking the slope between 0.1 and 0.3 % strain (ca. 25 % of failure strain). Statistics used include the mean (*x bar*), standard deviation (s_{n-1}) and the coefficient of variation (*COV*):

---

[7] See Appendix B for a sample calculation.

$$\bar{x} = \left(\sum_{i=1}^{n} x_i\right) \Big/ n \tag{4.3}$$

$$s_{n-1} = \sqrt{\left(\sum_{i=1}^{n} x_i^2 - n\bar{x}^2\right) \Big/ (n-1)} \tag{4.4}$$

$$COV = 100 s_{n-1} \Big/ \bar{x} \tag{4.5}$$

Interlaminar Shear Testing Along the Fiber Direction (ASTM D 2344 - 84): Rectangular specimens were cut from composite panels using a fine bandsaw and measured 5 cm (2 inches) long, 0.625 cm (0.25 inches) wide and ca. 4 mm in thickness. Short beam shear tests were performed using an Instron Testing Machines model 4204 with a load beam of 5 kN in a laboratory environment. The crosshead speed was kept at 1.3 mm/min for all tests. The span used was kept constant at 19.05 mm. The tests were conducted at room temperature. Reported data points represent the average of 10 measurements. Test specimens were conditioned at room conditions for greater than 40 hours. The apparent shear strength (s_H) was calculated using the following equation:

$$s_H = 0.75 P_B \Big/ bd \tag{4.6}$$

where: b = width of specimen
d = thickness of specimen
P_B = breaking load

Statistics used include the mean, standard deviation and the coefficient of variation (Equations (4.3-5), respectively).

Experimental Design: The Box-Behnken experimental design was chosen to model the consolidation process. This design includes the depicted points within the design space (Figure 4.2). For three variables (1, 2, 3) and three levels per variable (-, 0, +), there are 13 test points (including the center point) as well as two more repetitions of the center point (total of 15 test conditions) (Table 4.1 and 4.2).

Design of experiments (DOE) software included in Schmidt and Launsby [1994] was used to fit the experimental data including all linear effects of each variable, all linear interaction effects between variables and all factor effects of each variable. Output includes all regression model coefficients as well as probabilities regarding whether or not that parameter belongs in the model. Also included in the output are the R^2 value of the fit and the model standard deviation.

Both the void volume as well as the apparent interlaminar shear strength (ILSS) experimental observations were analyzed using DOE techniques with the intention of predicting the set of consolidation conditions which would minimize the void volume content of composites and maximize the ILSS.

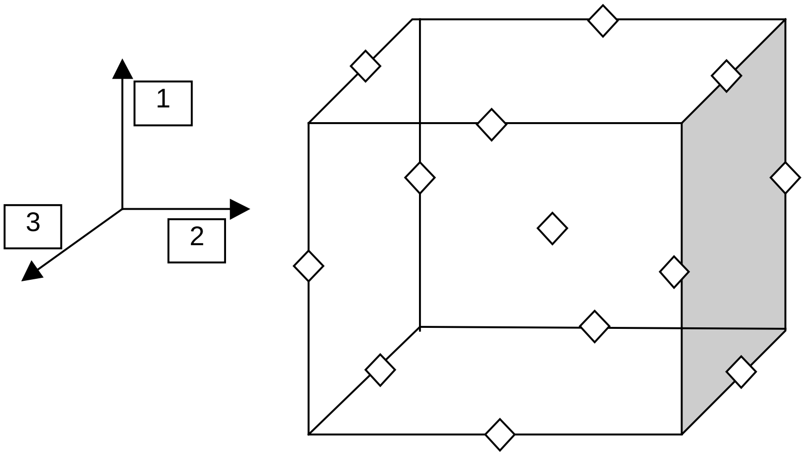

Figure 4.2 Box-Behnken Experimental Test Points.

Table 4.1 Box-Behnken Experimental Design (nonrandomized).

Run	A	B	C
1	-	-	0
2	-	+	0
3	-	0	-
4	-	0	+
5	0	-	-
6	0	-	+
7	0	+	-
8	0	+	+
9	0	0	0
10	0	0	0
11	0	0	0
12	+	-	0
13	+	+	0
14	+	0	-
15	+	0	+

Table 4.2 Variables and Levels Used.

Level	A. Temperature (°C)	B. Pressure (p.s.i.)	C. Time[8] (min.)
-	170	11.8	3
0	200	23.7	8
+	230	35.5	13

Scanning Electron Microscopy (SEM): SEM of the composite specimens was performed using an AMRAY 180 D (Diffusion system) Scanning Electron Microscope, at an operating voltage of 10 kV. Fracture surfaces of selected composites were mounted on an aluminum surface and sputter coated with gold in a Denton vacuum DV 515 evaporator.

4.3 Results and Discussion.

4.3.0 Composite Characterization.

Composites containing lyocell fiber tow along with CAB were prepared according to the procedures outlined in the methods section. The original fiber was white but thereafter emerged from the consolidation process with a golden to brown color, depending on the thermal severity and duration of the consolidation process. Figures 4.3 and 4.4 depict the prepregged panels before and after consolidation. This may be attributed to thermal degradation of the reinforcing fiber, which typically occurs during temperatures in excess of 200 °C. This process can be chemically interpreted as the decomposition of the glycosyl units to form char [Jain *et al*. 1987]. The cellulose ester matrix most likely does not undergo appreciable decomposition within the temperature ranges studied [Huang and Li 1998].

The panels produced had the characteristics outlined in Table 4.2. Composite fiber volume content ranged from ca. 52 to 68 % (voidless basis). Fiber volume fraction determination using GC was verified by the determination that the CAB had a 34 to 36 wt% butyryl ester content, which agrees reasonably well with the stated manufacturer's value of 38 wt% butyryl ester.

The lowest void content observed was for the consolidation condition of 200 °C, 11.8 p.s.i. pressure and a time of 13 minutes (2.83 % void content)[9]. The highest void content was observed at 170 °C, 23.7 p.s.i. and a time of 3 minutes (25 % void content).

---

[8] All composites were first laid in the press under vacuum with no pressure on the platens for two minutes prior to application of pressure for the indicated time.

[9] In this case, panel 11 had a void content of 0.01 % lower; however, this value is not representative due to the fact that the two other panels 9 and 10 were produced at the same conditions yet showed void contents of ca. 5 %.

Figure 4.3 Prepreg Panel Before Consolidation.

Figure 4.4 Consolidated Composite Samples.

The experimentally determined void contents can be depicted as strictly functions of temperature, pressure and consolidation time (Figures 4.5-7). Figure 4.5 depicts void volume as a function of consolidation temperature while the other consolidation variables were held constant (at the values indicated in the graph legend). From this graph, it does not seem clear exactly how void volume correlates with consolidation temperature. Two lines suggest a negative correlation while two lines suggest a positive correlation. Three of the lines are of small slope; however, for the 23.7 p.s.i. press pressure and 3 minute consolidation time, an increase in consolidation temperature from 170 °C to 230 °C reduced the void volume from 25 to 11 volume %. Examination of just the experimental results however can be misleading. For example, a minima or maxima[10] in the interior of the curves depicted in Figure 4.5 could remain undetected. Therefore, the exact nature of the temperature dependence of the void content can not be fully understood without fitting all of the experimental data with the regression model. To this extent, it must be understood that Figures 4.5-7 merely represent limited experimental data and may only give *indications* of any data trends.

---

[10] Could be expected for instance in temperature with lower and upper limits of high melt viscosity and material thermal degradation, respectively.

Table 4.2 General Characteristics of Composites Produced.

Composite Specimen Number	Butyryl Pyrrolidine Content (mg)	Fiber Volume Content (%, Voidless Basis)	Void Content (%)
1	26.1	54	8
2	24.7	56	6
3	27.3	52	25
4	23.6	58	11
5	22.8	59	22
6	25.1	60	3
7	23.1	64	11
8	24.7	62	6
9	23.6	63	5
10	20.7	68	5
11	24.4	59	3
12	21.6	64	10
13	23.1	63	11
14	24.6	59	11
15	21.7	64	8

	Press Temp. (°C)	Press Pressure (p.s.i.)	Press Time (min.)			
1	170	11.8	8			
2	170	35.5	8			
3	170	23.7	3			
4	170	23.7	13			
5	200	11.8	8			
6	200	11.8	13			
7	200	35.5	3			
8	200	35.5	13			
9	200	23.7	8			
10	200	23.7	8			
11	200	23.7	8			
12	230	11.8	8			
13	230	35.5	8			
14	230	23.7	3			
15	230	23.7	13			

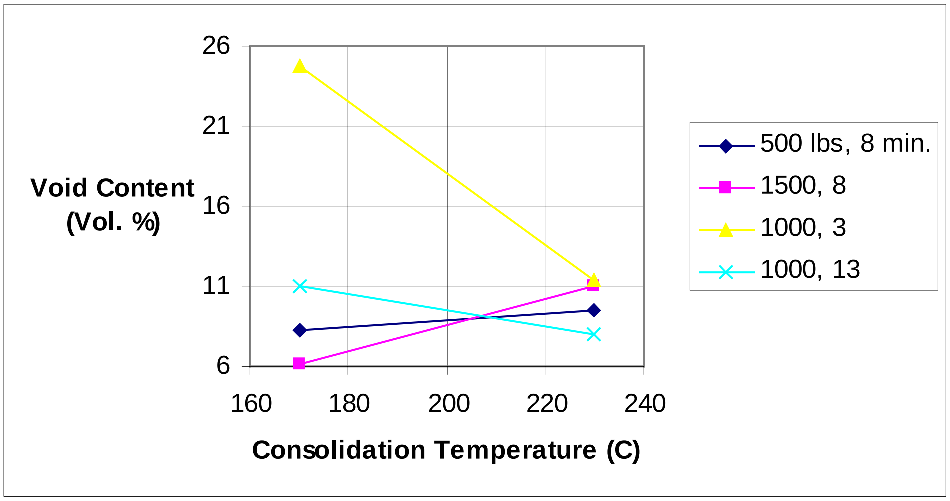

Figure 4.5 Void Volume of Composites as a Function of Consolidation Temperature (other variables constant).

Figure 4.6 depicts the void volume of the composites produced as a function of consolidation pressure. It can be seen that two lines show an increase in void volume while two lines show a decrease in void volume with increasing consolidation pressure. Pressure does not seem to have a definite effect on void volume of the composites produced. However, the same disclaimer regarding possible maxima or minima on the interior of the curves depicted applies here as well.

Figure 4.7 depicts the void volume of the composites produced as strictly a function of consolidation time. All four lines show that void volume tended to decrease as the consolidation time increased. This effect was most evident for the consolidation condition of 200 °C and 11.8 p.s.i. total pressure. For a consolidation time increase from 3 to 13 minutes, the void volume dropped from 22 to 3 %.

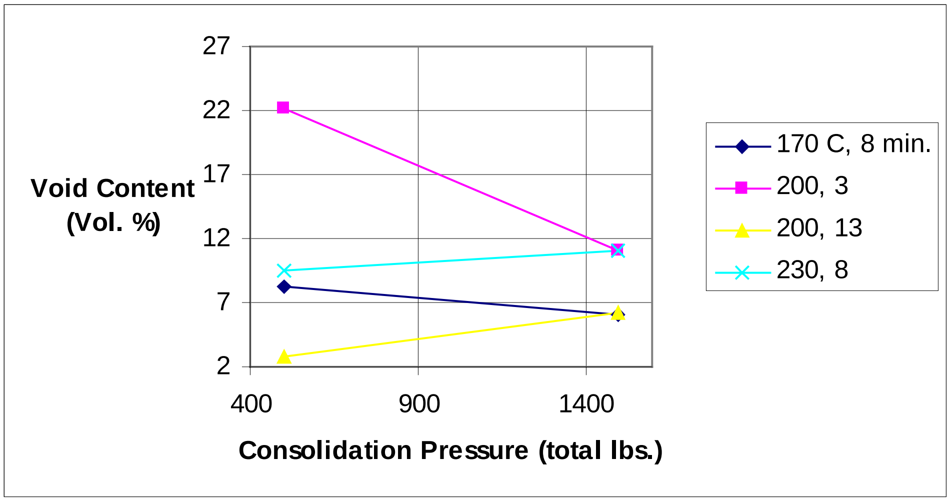

Figure 4.6 Void Volume of Composites as a Function of Consolidation Pressure (other variables constant).

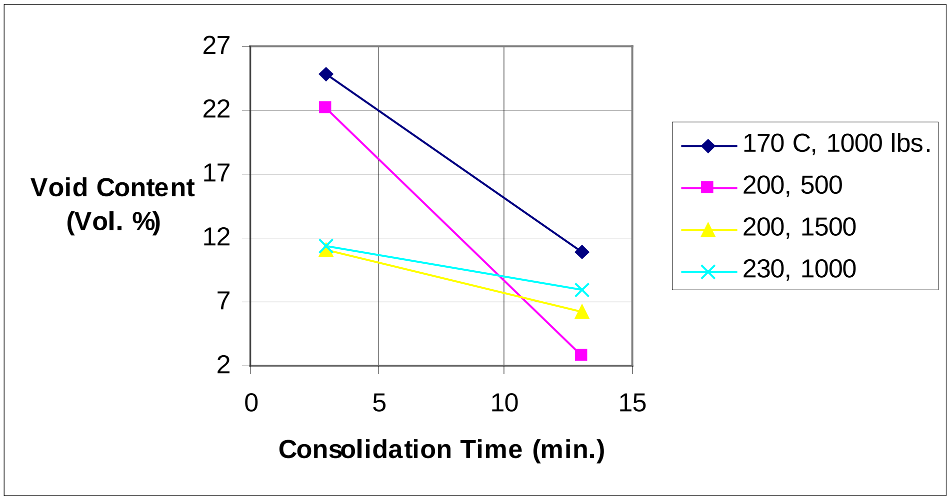

Figure 4.7 Void Volume of Composites as a Function of Consolidation Time (other variables constant).

4.3.1 Composite Tensile Properties.

Composite specimens were tested in stress strain mode along the fiber direction for both unacetylated fiber composites and acetylated fiber composites. A typical load strain curve for the composites produced is detailed in Figure 4.8. The response was nearly linear throughout the test duration.

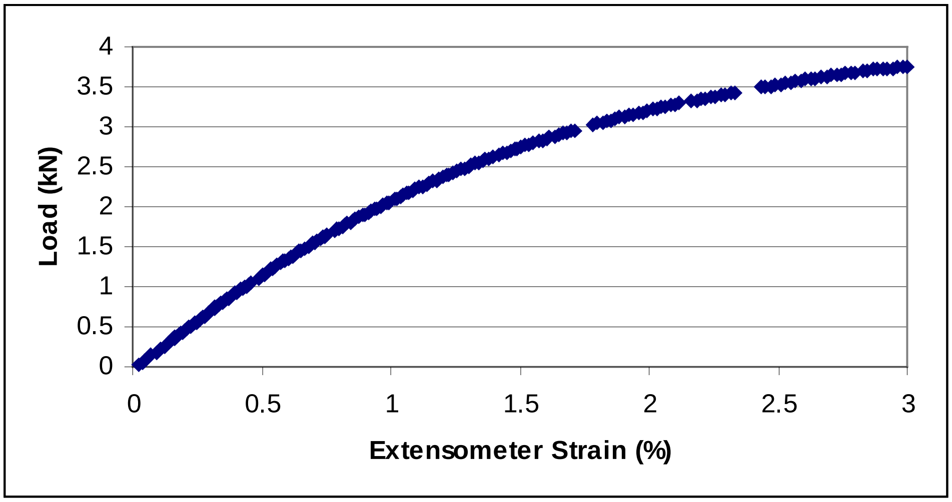

Figure 4.8 Typical Tensile Load Strain Curve for Composites Produced.

The tensile modulus, ultimate strength and ultimate strain are tabulated in Table 4.3. Moduli typically ranged from 18 to 20 GPa roughly depending on fiber content. Maximum strength values typically were centered around 200 MPa; however, this value is lower than the true value due to grip effects[11], voids, and the presence of stitching within the composite panels. The tensile specimen geometry is rectangular - therefore grip effects will tend to lower the ultimate strength of the material being tested. The stitching, present perpendicular to the loading direction also tends to lower the ultimate strength of the material because it acts as a flaw.

From these results, it appears that darkening of the fibrous reinforcement due to exposure to excessively high heat (i.e., 230 °C) does not cause a noticeable decrease in the tensile properties of the composites produced[12]. Although the mean ultimate strength as well as ultimate strain values tended to decrease at higher temperatures, most of these values are still within one standard deviation of the values at other consolidation temperatures.

---

[11] Grip effects meaning the crushing effect near the grips attained at high loads.

[12] See footnote on Page 65.

Table 4.3 Tensile Properties of Composite Panels[13].

Sample Number	Modulus (GPa)	Std. Dev.	Max. Strength (MPa)	Std. Dev.	Max. Strain (%)	Std. Dev.
1	18.2	3.6	210	14	2.10	0.39
2	18.1	1.0	229	18	1.87	0.22
3	10.8	2.2	120	11	1.92	1.05
4	18.6	3.2	194	16	1.75	0.44
5	17.4	1.1	221	11	1.97	0.27
6	21.6	1.3	246	27	1.72	0.35
7	18.4	4.7	203	26	1.81	0.14
8	18.1	1.2	204	26	1.68	0.20
9	19.3	3.1	215	33	1.48	0.19
10	20.4	0.9	211	20	1.52	0.16
11	18.4	3.4	201	22	1.73	0.29
12	18.5	4.1	184	29	1.15	0.31
13	17.3	2.5	187	19	1.40	0.14
14	16.4	2.2	177	31	1.52	0.35
15	18.9	1.5	170	20	1.12	0.23
	Press Temp. (°C)	**Press Pressure (p.s.i.)**	**Press Time (min.)**	**Fiber Volume (%, voidless basis)**	**Void Volume (%)**	
1	170	11.8	8	54	8	
2	170	35.5	8	56	6	
3	170	23.7	3	52	25	
4	170	23.7	13	58	11	
5	200	11.8	8	59	22	
6	200	11.8	13	60	3	
7	200	35.5	3	64	11	
8	200	35.5	13	62	6	
9	200	23.7	8	63	5	
10	200	23.7	8	68	5	
11	200	23.7	8	59	3	
12	230	11.8	8	64	10	
13	230	35.5	8	63	11	
14	230	23.7	3	59	11	
15	230	23.7	13	64	8	

---

[13] With the exception of panel 3, the other panels are not statistically different. For example, using a t-test (alpha = 0.05), it can be shown that panel 14 has the 'same' tensile properties as panel 2.

4.3.2 Composite Interlaminar Shear Strength.

The composites produced all failed in horizontal shear for the span used in this study. The apparent interlaminar shear strengths (ILSS) of the composites produced are depicted in Table 4.4 and a sample load vs. displacement curve is shown in Figure 4.9.

The ILSS typically ranged from 10 to 14 MPa. The highest ILSS (15.5 MPa) was produced by two composites: 1) 200 °C, 11.8 p.s.i. and 13 minutes, and 2) 200 °C, 23.7 p.s.i. and 8 minutes.

The experimental data for the ILSS can be examined as strictly a function of consolidation temperature, pressure and time (as was the void volume data). However, the same cautionary statement applies as in the void volume data: this is limited experimental data and must be treated as such. A more complete mathematical analysis using the entirety of the data will be carried out in the next section on the void volume and ILSS regression models. Figures 4.10-12 depict ILSS as a function of consolidation temperature, pressure and time while keeping the other respective variables constant.

Figure 4.10 depicts the ILSS as a function of consolidation temperature. Although at first glance it appears that ILSS overwhelmingly increases with temperature, this trend is not significant because of the overlap in error bars for both points of each lines. The standard deviation for each point typically ranged from ca. 1 to 1.8.

Figure 4.11 shows the ILSS as a function of consolidation pressure. Increasing consolidation pressure seems to decrease the ILSS for the points shown; however, as in the case of temperature, the points also do not differ more than one standard deviation, indicating the insignificance of the trends according to the data shown.

The last figure of this series (Figure 4.12) shows ILSS as a function of consolidation time. It appears here that as the time of consolidation is increased, the ILSS increases. This trend is significant for the case of 170 °C, 11.8 p.s.i. and 200 °C, 35.5 p.s.i. The error bars do not overlap for the two endpoints. This indicates that there may exist a trend that shows increasing consolidation time increases the ILSS. However, until the regression analysis is completed, no conclusions should be drawn at this time.

Table 4.4 ILSS for the Composites Produced.

Sample Number	ILSS (MPa)	Std. Dev.
1	13.1	1.3
2	11.5	2.9
3	10.4	1.9
4	11.9	3.1
5	12.3	1.5
6	15.5	0.9
7	11.6	0.8
8	14.1	1.3
9	14.3	0.8
10	15.2	1.0
11	15.5	1.7
12	14.7	1.5
13	13.5	1.6
14	13.4	1.6
15	14.1	0.6

Sample Number	Press Temp. (°C)	Press Pressure (p.s.i.)	Press Time (min.)	Fiber Volume (%, voidless basis)	Void Volume (%)
1	170	11.8	8	54	8
2	170	35.5	8	56	6
3	170	23.7	3	52	25
4	170	23.7	13	58	11
5	200	11.8	8	59	22
6	200	11.8	13	60	3
7	200	35.5	3	64	11
8	200	35.5	13	62	6
9	200	23.7	8	63	5
10	200	23.7	8	68	5
11	200	23.7	8	59	3
12	230	11.8	8	64	10
13	230	35.5	8	63	11
14	230	23.7	3	59	11
15	230	23.7	13	64	8

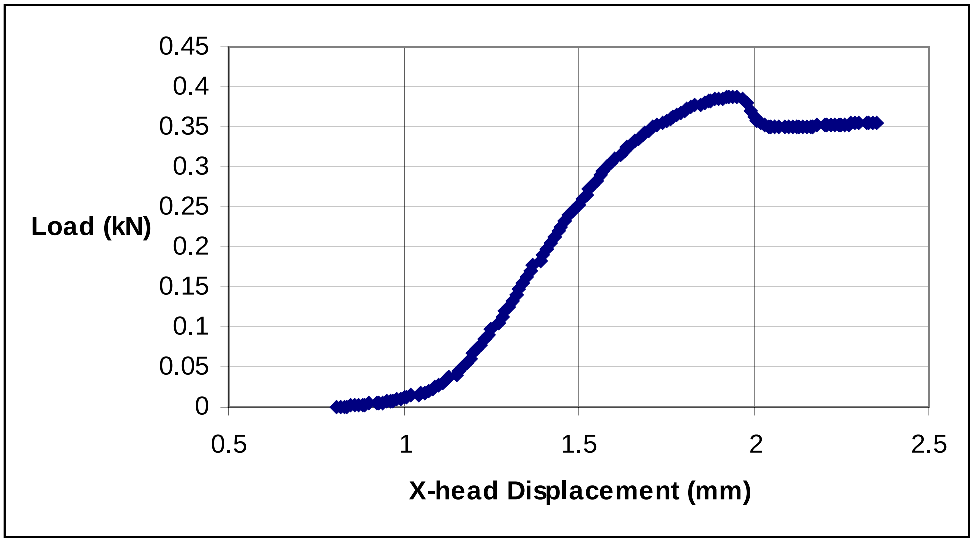

Figure 4.9 ILSS Load vs. Displacement Sample Curve.

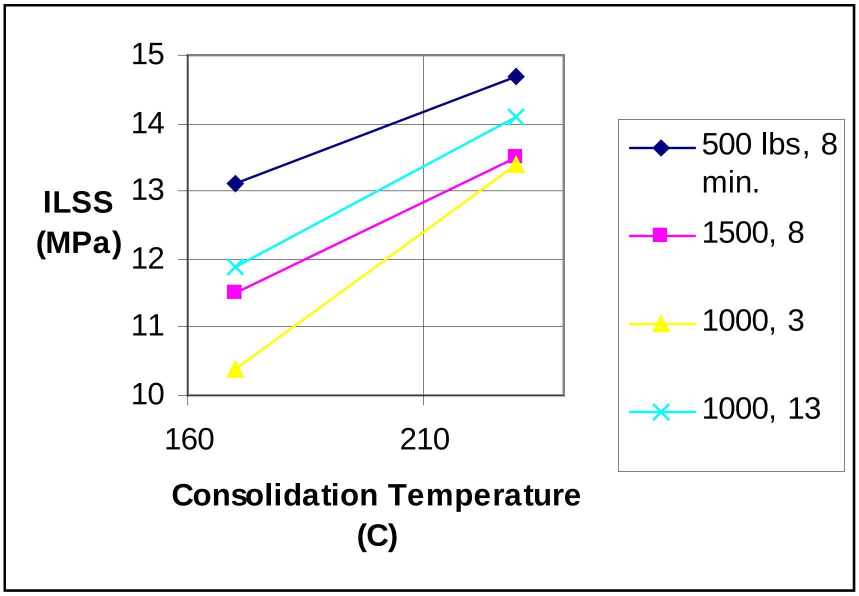

Figure 4.10 ILSS of Composites as a Function of Consolidation Temperature (other variables constant).

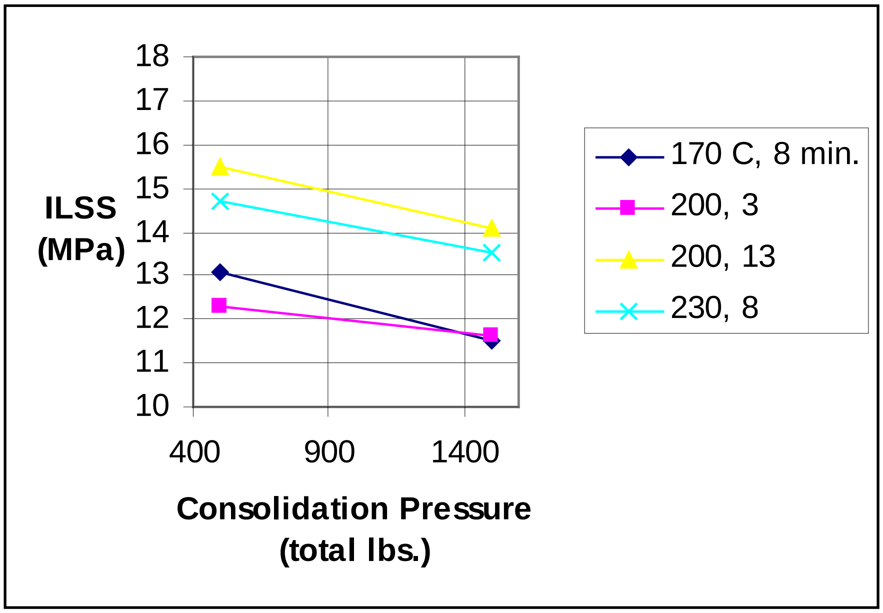

Figure 4.11 ILSS of Composites as a Function of Consolidation Pressure (other variables constant).

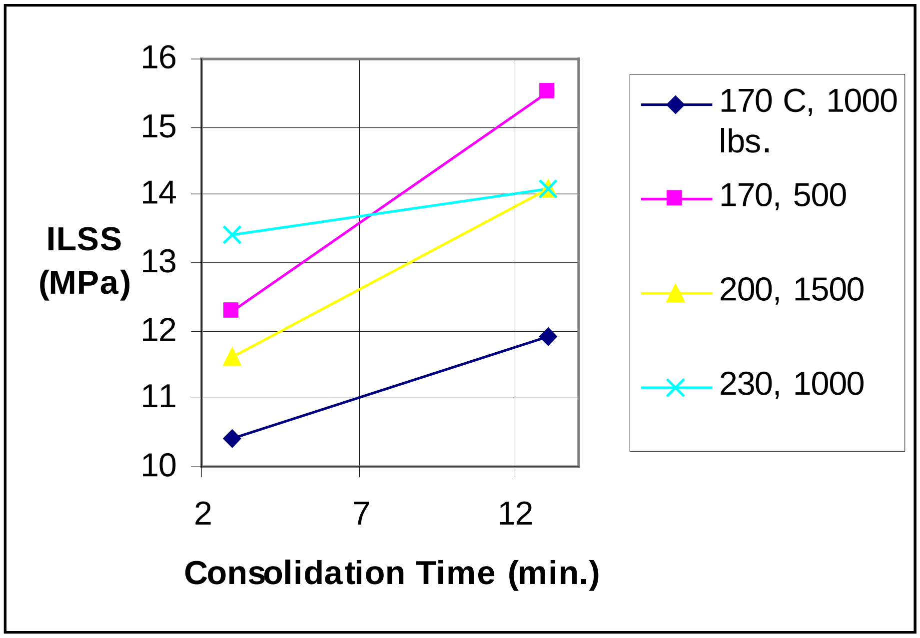

Figure 4.12 ILSS of Composites as a Function of Consolidation Time (other variables constant).

4.3.3 Regression Models for Void Volume and ILSS.

Void Volume Analysis: Using the fifteen data points for composite void volume as a function of consolidation conditions, a regression model was generated to predict void volume continuously throughout the design space. The model, which can account for linear effects, linear interactions and second order effects, is given in the following equation:

$$\begin{aligned} &Void\quad Volume\quad (\%) = 10.15 + 1.73T - 1.69P - 2.12t \\ &- 2.90TP + 3.59Tt + 1.57Pt + 3.68T^2 - 1.32P^2 - 3.26t^2 \end{aligned} \tag{4.7}$$

The variables in this case are all normalized to range from -1 to +1.

The R^2 value of this regression is 0.50, with a standard error of 7.44 void volume %. This indicates a relatively poor fit of the data (Figure 4.13). This is either an indication of poor fit using the equation (other effects such as other combinations of variables dominate) or a data source that is laden with noise. Noise then would most likely obscure any trends that the input variables have on void volume. Noise could either result from poor measurement technique or the presence of uncontrolled inputs to the composite fabrication process.

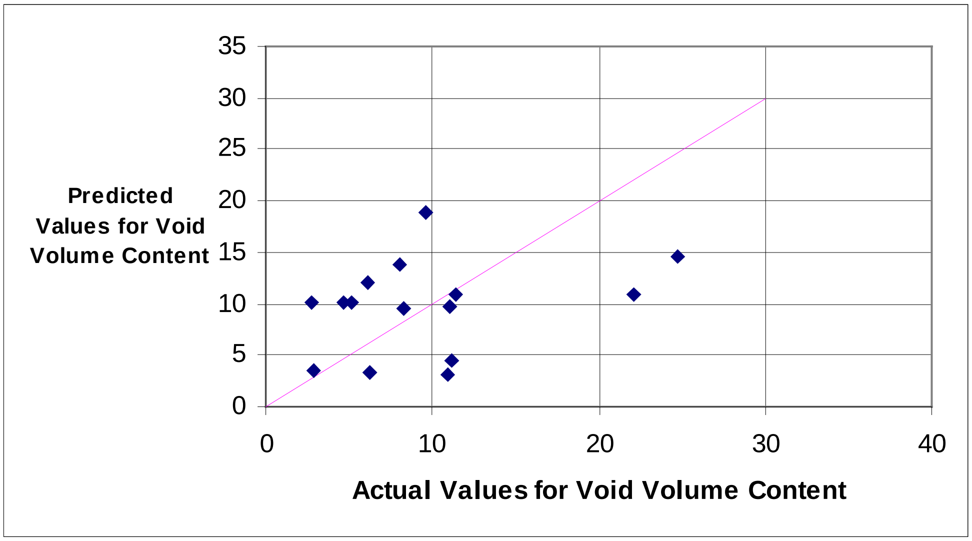

Figure 4.13 Comparison of Actual Void Volume Measurements with Predicted Quantities.

The coefficients of this equation are depicted in a Parato chart shown in Figure 4.14. The P(2 Tail) values, which represent a probability that the parameter belongs in the model, are shown in Table 4.5. A rule of thumb commonly used [Schmidt and Launsby, 1994] to determine whether or not a factor belongs within a regression model (i.e., has an orchestrated effect) is that its P(2 Tail) value must be less than 0.10. Using this rule, it appears that none of the input variables studied has an effect (linear,

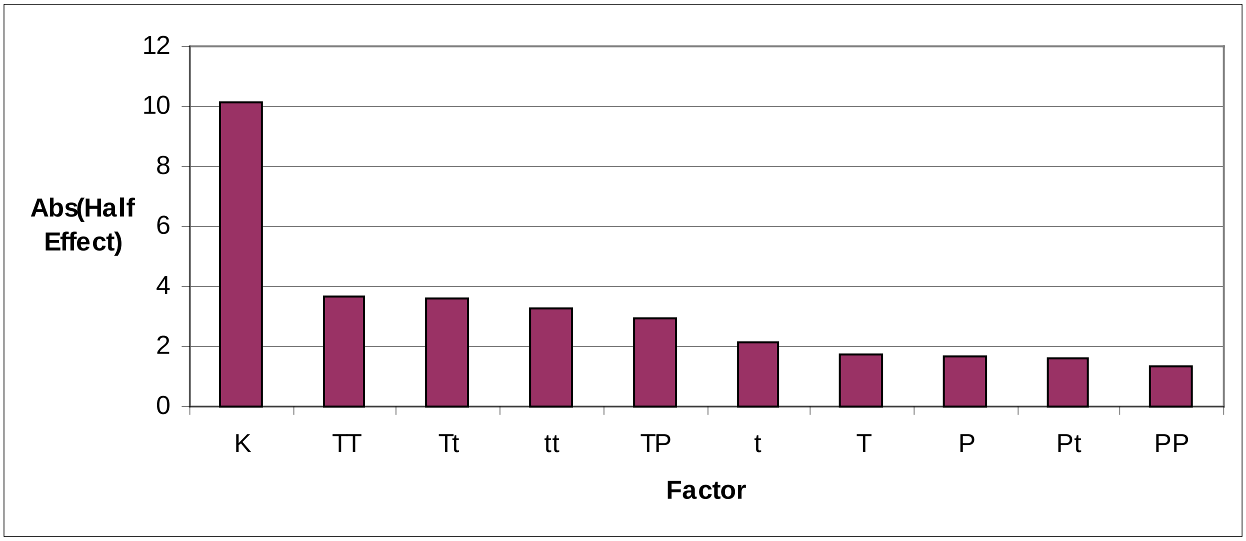

Figure 4.14 Parato Chart for the Absolute Values of Half Effects (for Void Volume).

Table 4.5 P(2 Tail) Values for the Half Effects in the Void Volume Regression.

Variable	P(2 Tail)
Constant	0.0645
T	0.5409
P	0.5488
t	0.4563
TP	0.4705
Tt	0.3785
Pt	0.6900
TT	0.3850
PP	0.7477
tt	0.4387

interactive, or second order effects) on void volume within the composite. In other words, the *measured* densities of the composites experienced considerable random fluctuation.

Using the regression model, an optimal point can be identified within the design space that minimizes void content. A minimum void content of -0.96 volume % can be found at the low temperature (170 °C), low pressure (11.8 p.s.i.) and high time (13 minutes) condition.

ILSS Analysis: The regression of the experimental data is depicted in the following equation:

$$\begin{aligned} ILSS \quad (MPa) &= 13.7 - 0.550T + 0.081P + 0.748t + 0.776TP - 0.175Tt - 0.423Pt \\ &- 1.74T^2 - 0.164P^2 + 1.45t^2 \end{aligned} \tag{4.8}$$

The variables in this case are also normalized to range between -1 and +1. Again, the regression model only considers linear effects, linear interaction effects and second order effects.

The R^2 value for this fit is again poor, 0.43, with a standard error of 1.72 MPa (Figure 4.15). As in the case of void volume, this indicates that there is considerable noise in the data. However, this does not rule out the possibility that the consolidation input variables significantly affect the output (ILSS, in this case). We must examine the P(2-Tail) values to see which variables should be included in our regression model and are significant.

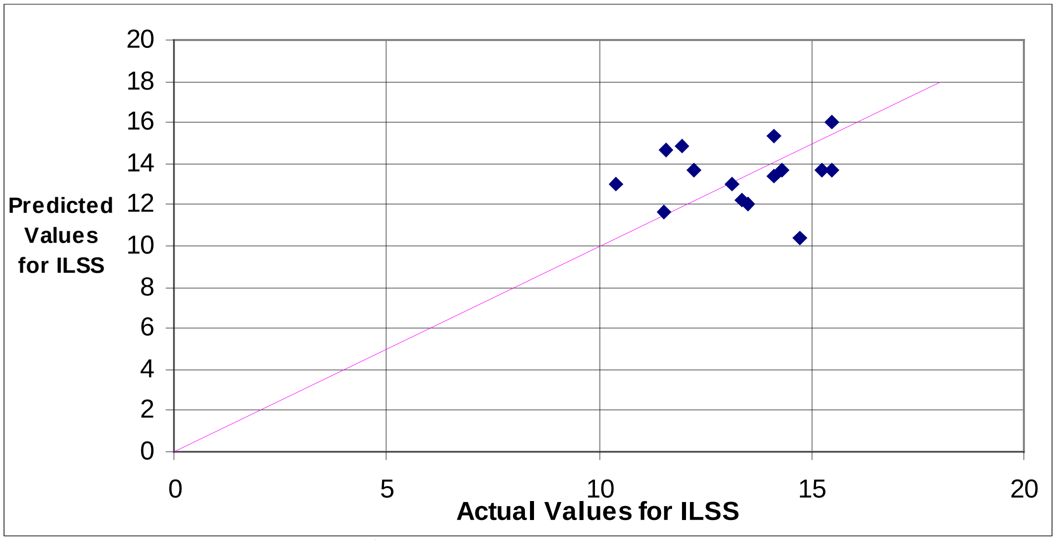

Figure 4.15 Comparison of Actual ILSS Measurements with Predicted Quantities.

The Parato chart for the absolute value of the half effects for ILSS is shown in Figure 4.16 and the corresponding P(2-Tail) values are given in Table 4.6. We apply the same rule of thumb as used before, and find that temperature, consolidation time, TP, TT and tt all seem to play an important role in determining ILSS.

Using the regression model for ILSS, an optimal ILSS of 18.3 MPa is calculated for a consolidation taking place at 187 °C, 11.8 p.s.i. and 13 minutes consolidation time.

This can be seen on the ILSS response surface generated while keeping pressure constant at 11.8 p.s.i. (Figure 4.17). The ILSS can be seen to increase with increasing consolidation time as well as decrease at the extremes of the design space. The optimal area (at this pressure, the apparent optimal pressure) to operate in is evident in the contour plot: all the way to the extreme long time condition and moderate temperature. This is a possible reflection of the limitations of using a high melt viscosity matrix melt, the upper limit on consolidation temperature being the degradation temperature of the fiber.

This phenomena may possibly be a reflection of the molecular interdiffusion process taking place at the boundaries of the prepreg stacked layers. As more press time is allowed for, more interdiffusion may be taking place, thus increasing the interlaminar shear strength between the plies.

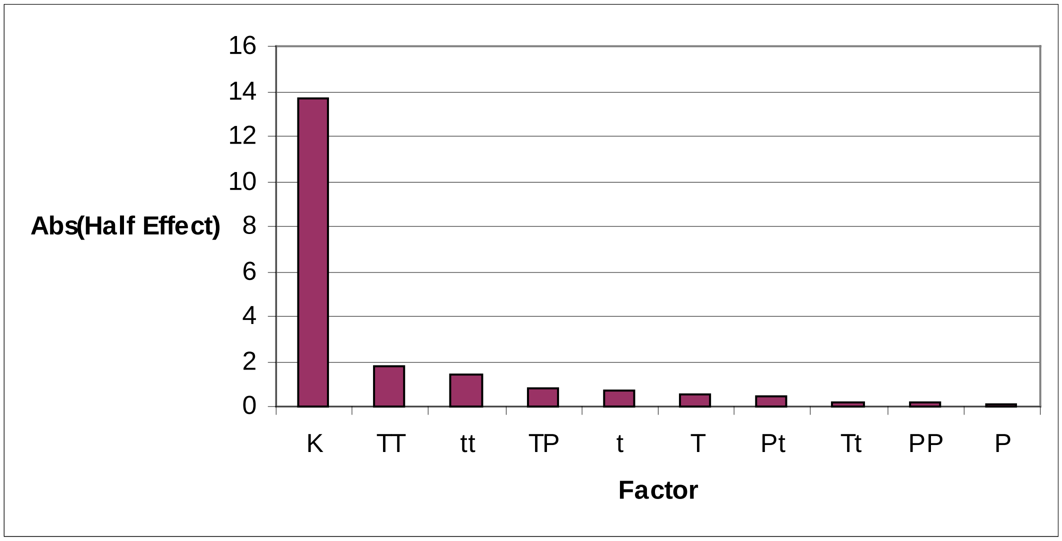

Figure 4.16 Parato Chart for the Absolute Values of Half Effects (for ILSS).

Table 4.6 P(2 Tail) Values for the Half Effects in the ILSS Regression.

Variable	P(2 Tail)
Constant	0
T	0.0049
P	0.675
t	0.0002
TP	0.0049
Tt	0.5215
Pt	0.1221
TT	0
PP	0.5625
tt	0

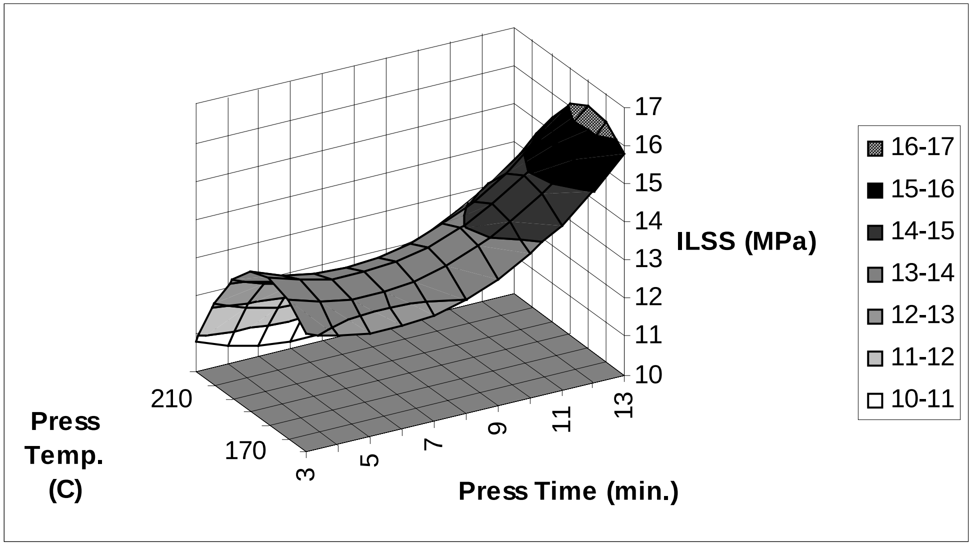

Figure 4.17 Response Surface for ILSS as a Function of
Consolidation Temperature and Time
(holding consolidation pressure constant at 11.8 p.s.i.).

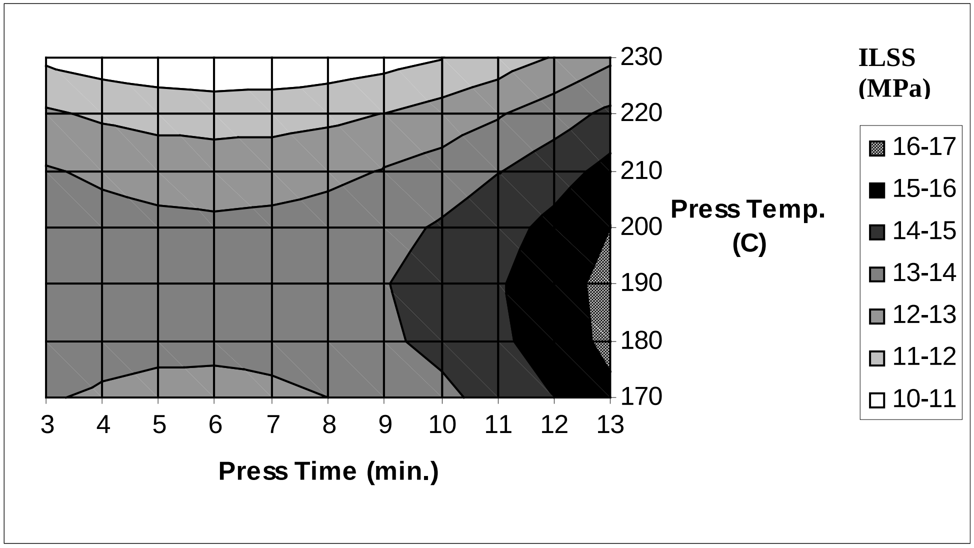

Correlation Between ILSS and Void Volume: The measured ILSS is negatively correlated with the measured composite void volume. This is illustrated in Figure 4.18. The prediction equations for ILSS and void volume also show a negative correlation between ILSS and void volume. This may possibly be an indication that high void volumes (most likely concentrated between the plies) lead to decreases in ILSS.

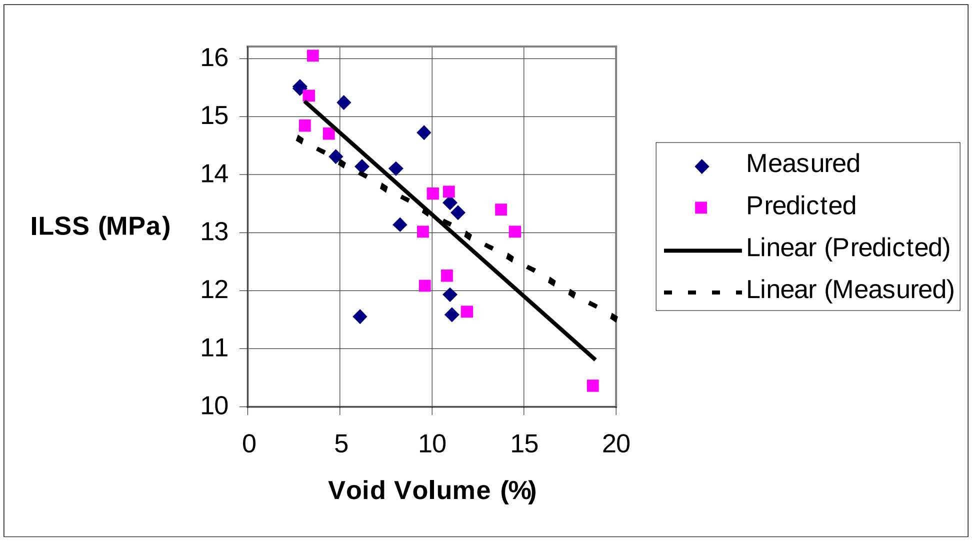

Figure 4.18 ILSS vs. Composite Void Volume.

4.3.4 SEM Visualizations of Selected Composite Fracture Surfaces.

A limited number of composite tensile fracture surface samples were randomly chosen in order to revisit the issue of interfacial adhesion between the matrix and fiber. These are depicted in Figure 4.19-21.

As can be seen from the dramatic illustrations below, fiber-matrix adhesion appears quite good. There are no indications that fiber surface modification is required for adequate stress transfer to occur between the fiber and matrix (concurrent with the conclusion from Chapter 3). Figure 4.19 shows relatively little fiber pull-out during fracture. In Figure 4.20, bundles of fibers show extensive amounts of fractured matrix particles adhering to the fiber surface (i.e., cohesive failure of the matrix). In sample number 4 (Figure 4.21), it is even evident that matrix spreads over the fiber and adheres to the surface.

4.4 Conclusions.

In summary, design of experiments was employed in order to minimize composite void volume as well as maximize interlaminar shear strength (ILSS) in the cellulose fiber/CAB composite system. Composites were manufactured at differing consolidation temperatures, pressures and times according to Box-Behnken methodology. The fiber volume fraction, void volume fraction, tensile strength and ILSS were then measured for each composite. Afterwards, composite tensile fracture surfaces were examined using scanning electron microscopy.

Tensile property evaluation suggested that no significant decrease of tensile properties was experienced through the use of excessive melt temperatures (230 °C).

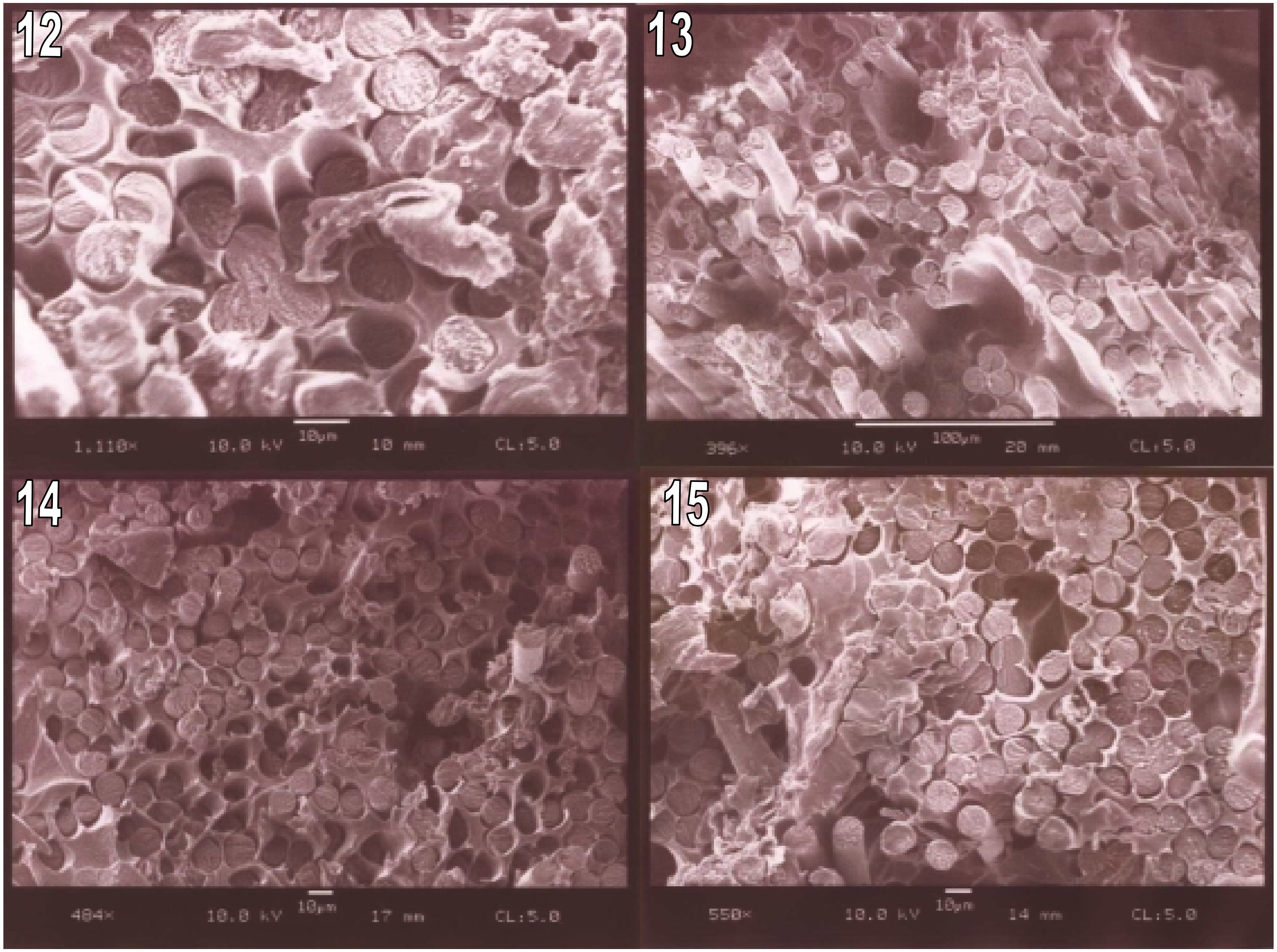

Figure 4.19 SEM Images of Tensile Fracture Surfaces of Selected Composite Specimens: Cross-Sectioned Failure (Numbers indicate Composite Panel Number).

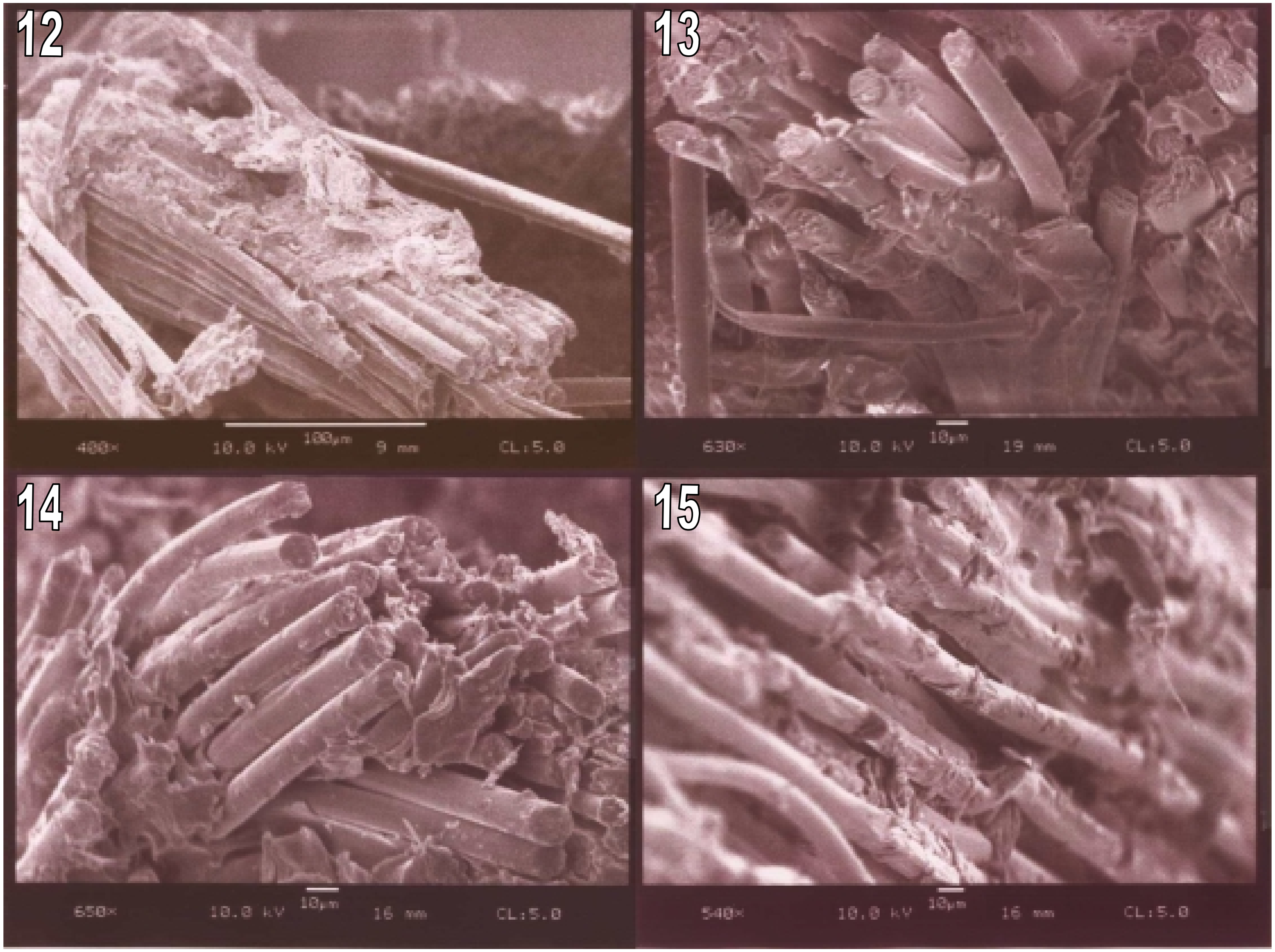

Figure 4.20 SEM Images of Tensile Fracture Surfaces of Selected Composite Specimens: Side View of Fiber Bundles Pulled Out (Numbers indicate Composite Panel Number).

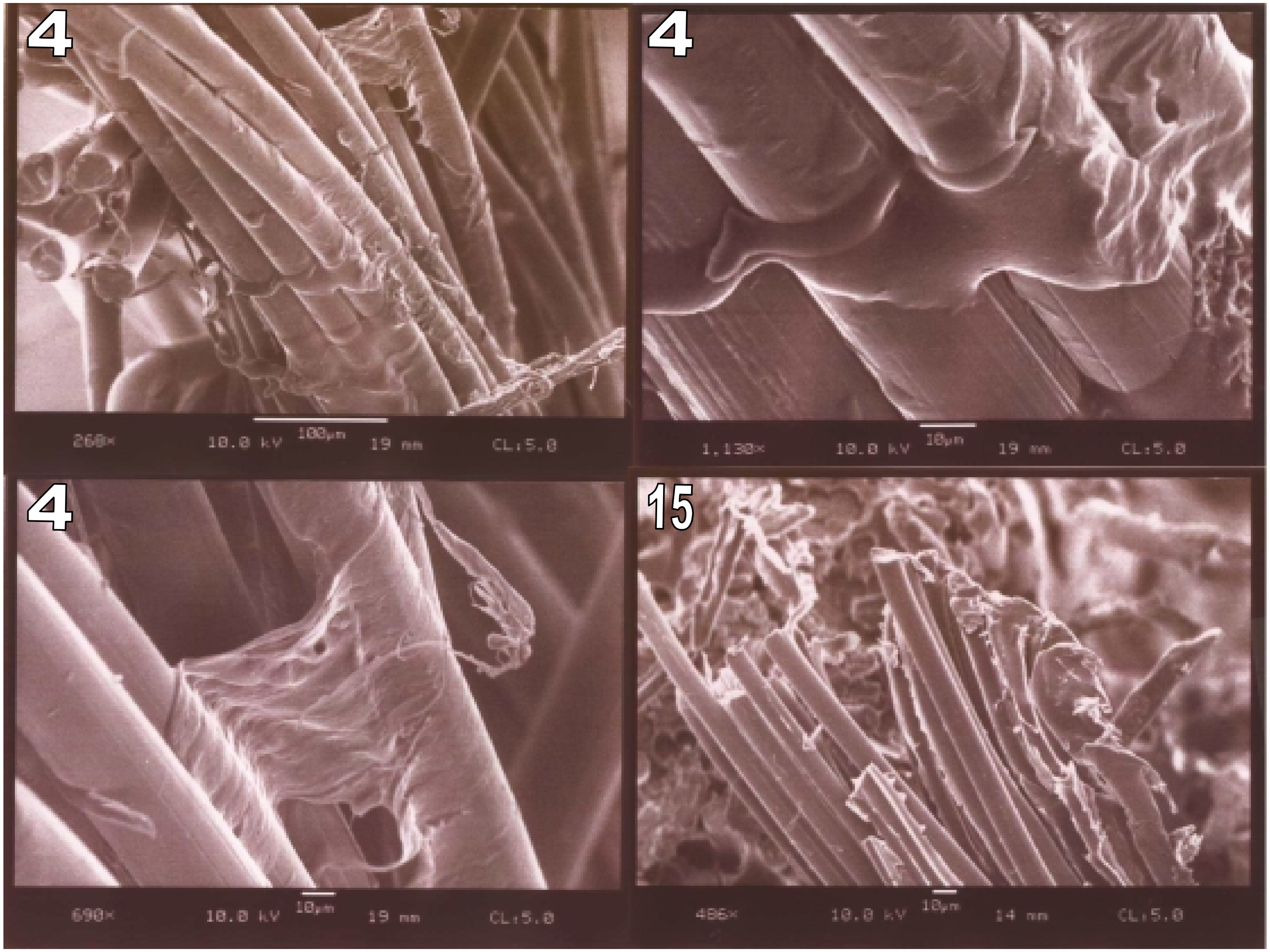

Figure 4.21 SEM Images of Tensile Fracture Surfaces of Selected Composite Specimens: Cohesive Failure in Pulled-Out Fiber Bundles (Numbers indicate Composite Panel Number).

Maximum strength values were typically in the range of 246 MPa while moduli values were ca. 22 GPa for a composite containing close to 3 volume % voids and 60 volume % fiber (voidless basis). Furthermore, microscopic evaluation revealed very little clean fiber pull out during composite fracture of both composites produced, suggesting relatively good fiber/matrix adhesion in both cases. Fractured matrix particles were seen to adhere relatively strongly to fiber surfaces, suggesting a considerable amount of cohesive failure. This observation is concurrent with other unmodified fiber composites manufactured in the previous chapter.

The properties of ILSS and void volume content were found to contain a large amount of noise and were highly variable. Optimization based on experimental observation ('pick the winner') and the use of regression techniques are reviewed in Table 4.7. The results obtained using both techniques are largely consistent; however, the lower optimal temperatures predicted by the regression model should be approached with caution (the fits were found to be relatively poor). Optimal conditions for composite consolidation appear to reside in moderate temperatures, low consolidation pressures and long consolidation times.

Table 4.7 Optimization of ILSS and Composite Void Volume.

Optimization Technique	Void Volume	ILSS
Optimization Based on Experimental Results	200 °C, 11.8 p.s.i., 13 minutes; 2.83 %	200 °C, 11.8 p.s.i., 13 minutes; 15.5 MPa
Optimization Based on Regression Modeling	170 °C, 11.8 p.s.i., 13 minutes; -0.96 %	187 °C, 11.8 p.s.i., 13 minutes; 16.3 MPa

CHAPTER 5.

Future Work.

This work was commissioned to further develop the polymer composite system consisting of cellulose acetate butyrate (CAB) and high modulus, continuous, regenerated cellulose fiber (lyocell). The two experimental studies dealing with composite development have resulted in two main conclusions: 1) interfacial adhesion appears to be good without the need for fiber surface modification, and 2) void formation within this composite system can be extensive (frequently > 5 volume % voids) due to the difficulties in consolidating this composite due to the relatively high viscosity of the matrix melt.

Interfacial adhesion was found to be substantial due to the relative lack of the fiber pull-out phenomenon during tensile failure noted in the unmodified fiber composites. This result was then supported in the second study in which similar unmodified fiber composites experienced very little fiber pull out with evidence of a large amount of fractured matrix particles adhering to the fiber surfaces.

Void volume formation was mitigated to a small extent by the use of optimal consolidation conditions. Composites formed at moderate temperature, low consolidation pressure and high consolidation times were found to have the lowest void formation. These composites were generally found to have the highest interfacial shear strength.

The highly variable nature of measured void formation should continue to be the focus of further investigations. Further attempts should be made to reduce void formation in all steps of the composite manufacturing process. The formation of voids during consolidation as well as during solution prepregging should continue to be of interest.

Solution prepregging typically results in void formation within the prepregs simply because of the nature of the evaporative drying process. As outer layers rid themselves of solvent, they tend to increase in viscosity as the polymer fraction approaches one. This typically leaves the inner layers of the prepreg tow (not yet dry) with no (expedient) way to remove solvent. Therefore, this results in solvent bubbles formed within the prepregs.

In addition, during the consolidation process, it is suspected that voids are formed due to the joining of two or more plies. Air pockets become trapped between the plies due to the roughness of the surfaces, and thus should be removed by consolidation. However, due to the limited extent at which the matrix can rid itself of voids (due to the high viscosity), precedence has to be placed on void *prevention* efforts rather than accumulating voids and then expecting to ‘melt’ them out during consolidation. An illustration of this concept would be to individually press each panel to remove surface irregularities, and then to join ‘prepressed’ panels together. This kind of strategy will be needed to avoid forming voids simply by joining panels together in a haphazard manner.

The matrix melt viscosity is also of enormous concern regarding the removal of voids during consolidation. Reducing this viscosity by way of process conditions is limited due to the degradation of the composite constituents. Therefore, other methods should be used to reduce melt viscosity. Both internal and external plasticization of the cellulose ester matrix should be considered. Externally plasticized cellulose acetate butyrate is commercially available (*Tenite Butyrate*, Eastman Chemical Company); however, internally plasticized cellulose esters (such as long chain cellulose esters) would have to be manufactured on a pilot scale. Both would have to be examined within the context of composites to see how: 1) the reduction in melt viscosity contributes to a reduction of void volume, 2) the interfacial behavior between the fiber and matrix changes and 3) the mechanical properties change with changing matrix polymer.

Removing voids is a very important step in the composite design process. Voids typically have a detrimental effect on composite mechanical properties, such as ultimate strength. Voids can also increase the variability of the final product. Some properties, however, are not highly affected by voids, such as modulus behavior. If a particular application is known to be modulus sensitive rather than ultimate strength sensitive, and if all (reasonable) efforts are made to remove voids within this system and an appreciable amount still remain, then the *void distribution* should then be characterized. Questions about the void distribution directly concern variability in the mechanical properties of the composites produced, and should thus be addressed prior to scale-up of the manufacturing process.

Another issue that should be considered is the determination of the true composite tensile strength. As was previously mentioned, these composites were tested using rectangular specimens and with deliberate imperfections in them (stitching). Manufacturing efforts should first qualify whether or not stitching is *required* at the optimal pressing condition to prevent fiber dealignment. Not using stitching in later composite production has the potential of increasing the tensile strength considerably. Furthermore, cutting specimens with grip tabs on them should also aid in the elucidation of the true tensile strength of these materials.

A comparison of these materials with other biobased and synthetic composites is outlined in Table 5.0. The first row represents the same matrix material used in this study combined with acetylated, discontinuous, steam exploded wood fiber. This resulted in a tensile modulus of just under 1 GPa and an ultimate strength of 16 MPa. Using a similar matrix material (PHB-V), Bourban *et al.* was able to incorporate continuous lyocell cellulose fibers into a composite to produce a material with dramatically increased tensile properties. Both modulus and strength increase more than an order in magnitude, even for a composite with reduced fiber content. Lastly with the composites produced in the current study, the fiber volume fraction was increased to produce a composite with twice the tensile modulus (but lower ultimate strength due to grip and artifact effects). A

Table 5.0. Comparison of Present Materials with Other Thermoplastic Composites.

Composite	**Fiber Volume Fraction**	**Tensile Modulus (GPa)**	**Tensile Strength (MPa)**
CAB/Steam Exploded Fiber[14]	0.40 (w/w)	0.84	16
PHB-V/Lyocell[15]	0.27 (w/w)	11.4	278
CAB/Lyocell[16]	0.62	22	246
Polyetherimide/Glass[17]	0.54	26	643
Polyetherimide/Carbon[4]	0.55	51	711

modulus of 22 GPa was obtained, which now places these composites within range of lower-end synthetic thermoplastic glass fiber composites.

Potential applications of these materials include applications in the transportation, sporting good, packaging and similar industries. These are where strong and lightweight materials are desirable. Because of the thermoplastic nature of these materials, they are relatively reusable, reshapable and repairable when compared with their thermosetting counterparts. Lastly, these composites are manufactured from a renewable source and are biodegradable, which is of key concern when considered in a sustainable economic framework.

---

[14] Glasser *et al.*, 1999.
[15] Bourban *et al.*, 1997.
[16] Present work.
[17] Hancox, 1989.